

Diploma Thesis

Thermo-Structural Behavior of Cryogenic Tanks During Cooldown: A Comparison Between Analytical and Numerical Methods

submitted in satisfaction of the requirements for the degree

Diplom-Ingenieur

of the TU Wien, Faculty of Mechanical and Industrial Engineering

Diplomarbeit

Thermostrukturelles Verhalten kryogener Tanks während der Abkühlung: Ein Vergleich zwischen analytischen und numerischen Methoden

ausgeführt zum Zwecke der Erlangung des akademischen Grads Diplom-Ingenieur eingereicht an der TU Wien, Fakultät für Maschinenwesen und Betriebwissenschaften

Juan Esteban Arjona Rodriguez, BSc

Matr.Nr.: 12402586

Betreuung: Univ.Prof. Mag. Dr. Yury Vetyukov

Institut für Mechanik und Mechatronik Forschungsbereich Mechanik fester Körper

Technische Universität Wien

Karlsplatz 13, 1040 Wien, Österreich

This work has been supported by AIT Austrian Intstitue of Technology within the framework of the Horizon Europe project ALRIGH2T (Airport-Level Demonstration of Ground refuelling of Liquid Hydrogen for Aviation; Grant agreement ID: 101138105).

I confirm, that the printing of this thesis requires the approval of the examination board.

Affidavit

I declare in lieu of oath, that I wrote this thesis and carried out the associated research myself, using only the literature cited in this volume. If text passages from sources are used literally, they are marked as such.

I confirm that this work is original and has not been submitted for examination elsewhere, nor is it currently under consideration for a thesis elsewhere.

I acknowledge that the submitted work will be checked electronically-technically using suitable and state-of-the-art means (plagiarism detection software). On the one hand, this ensures that the submitted work was prepared according to the high-quality standards within the applicable rules to ensure good scientific practice "Code of Conduct" at the TU Wien.

On the other hand, a comparison with other student theses avoids violations of my personal copyright.

Place and Date	Signature

Acknowledgments

My deepest thanks go to Univ.Prof. Mag. Dr. Yury Vetyukov for his invaluable supervision and insightful technical discussions. His guidance helped steer my thesis in the right direction, and I always left our meetings having learned something new.

I would like to express my sincere gratitude to Senior University Lecturer Jouni Freund for his generous and comprehensive support. Without his expertise in solid mechanics and the clarity of his explanations, this study would not have been possible.

I am also grateful to all my colleagues in the Simulation Group at the Austrian Institute of Technology for their continuous support throughout my thesis. I appreciated the opportunity to work on a real-world engineering problem, and the mentoring in software use, as well as the many technical discussions, were tremendously helpful.

I would like to thank the European Institute of Technology (EIT) for providing the scholarship that made this journey possible —one that began in France, continued in Finland, and concluded in Austria. Three countries, three languages, all different from my own. An experience I never imagined myself having.

To my parents and my brother: thank you for your constant encouragement and love. Even from afar, you always stayed close to my heart and took interest in my progress. Your support pushes me to strive to be a better person every day. ¡Los quiero con todo mi corazón!

This document is the result of several months of dedicated work and I am proud of it. Along the way, I've deepened my fascination with structural mechanics. Is it a complex field? Absolutely. Do I always grasp every derivation and equation? Not quite. But I've come to understand that engineering often means dealing with problems we don't fully comprehend—at least not yet. What matters is knowing how to move forward: by reading more, asking questions, and seeking guidance from those with greater experience.

To end, there is a word (my favorite one, in fact) in Spanish, my mother tongue. I've never quite managed to translate it: *el azar*. I want to thank *el azar* for the people it placed in my path, for the opportunities it offered me to grow into a better person and engineer, and for the curiosity and motivation it sparked in me to keep learning —day by day, little by little.

Kurzfassung

Kryogene Flssigwasserstofftanks sind whrend der Abkhlung am Boden erheblichen thermischen und mechanischen Belastungen ausgesetzt. In frhen Designphasen ist die Verwendung vollstndiger Finite-Elemente-Analysen (FEA) jedoch aufgrund des Rechenaufwands oft nicht praktikabel. In dieser Arbeit wird daher eine geschlossene, analytische Lsung entwickelt und validiert, wobei zugleich die Grenzen der Anwendbarkeit klassischer Strukturmechanik fr solche Probleme aufgezeigt werden.

Untersucht wurde ein horizontaler Zylinder aus Edelstahl 316L mit torisphrischen Bden, angelehnt an den Demonstrator aus dem Horizon-Europe-Projekt ALRIGH2T (Grant Agreement ID: 101138105). Der Tank wurde als dnnwandige zylindrische Schale idealisiert, um die Auswirkungen des Innendrucks zu erfassen, sowie als Euler-Bernoulli-Balken zur Abbildung von Schwerkraft und vertikal geschichteten thermischen Lasten. Umfangsspannungen infolge thermischer Gradienten wurden mittels zweidimensionaler Thermoelastizitt berechnet. Die Analyse erfolgte ber berlagerung, unter der Annahme linear-elastischen Materialverhaltens mit temperaturunabhngigen Eigenschaften. Das resultierende analytische Modell wurde mit detaillierten LS-DYNA-Simulationen verglichen, die Innendruck, idealisierte Flssigstickstoff-Temperaturgradienten und Eigengewicht bercksichtigen.

Das Schalenmodell sagte die Lngs- und Umfangsspannungen infolge des Innendrucks korrekt voraus. Auch das Balkenmodell erfasste die durch den vertikalen Temperaturgradienten verursachten Lngsspannungen sowie die Auswirkungen der Schwerkraft realittsnah wobei letztere sich im Vergleich zu Druck- und Thermospannungen als vernachlssigbar erwiesen. Das zweidimensionale thermoelastische Modell hingegen konnte die thermischen Umfangsspannungen in dieser Konfiguration nicht zuverlssig abbilden.

Die kombinierte analytische Formulierung bestehend lediglich aus Druck-Schalenmodell und thermischem Balkenmodell reproduzierte die Spannungsverteilung und Spitzenwerte mit einer Genauigkeit, die fr den Vorentwurf als ausreichend angesehen werden kann. In der Mitte des Zylinders wich die analytische von-Mises-Spannung nur um 1% vom FEA-Ergebnis ab, whrend die Spannungen an den Schweinhten konservativ berschtzt wurden. Diese Grenzberschtzung ist auf die vernachlssigte Elastizitt der torisphrischen Kappen zurckzufhren, welche das analytische Modell lokal versteiften.

Insgesamt zeigt diese Untersuchung, dass klassische Schalen- und Balkentheorien eine schnelle und hinreichend genaue Spannungsabschtzung in frhen Entwurfsphasen ermglichen, whrend gleichzeitig die Bereiche identifiziert werden, in denen hochauflsende Simulationen weiterhin erforderlich bleiben.

Abstract

Cryogenic liquid-hydrogen tanks are subjected to significant thermal and mechanical loads during ground cooldown. However, in early design phases, the use of full finite-element analysis (FEA) is often impractical due to its computational cost. This thesis therefore develops and validates a closed-form analytical alternative, while also delineating the limits of applicability of classical structural mechanics to such problems.

The study utilized a horizontal 316L stainless steel cylinder with torispherical heads, modeled after the demonstrator developed in the Horizon Europe project ALRIGH2T (Grant Agreement ID: 101138105). The tank was idealized as a thin cylindrical shell to capture the effects of internal pressure, and as an Euler-Bernoulli beam to represent gravity and vertically stratified thermal loads. Circumferential thermal stresses were evaluated using two-dimensional thermoelasticity. The response was analyzed through superposition, under the assumptions of linear elasticity and temperature-independent material properties. The resulting analytical model was benchmarked against detailed LS-DYNA simulations that included internal pressure, idealized liquid-nitrogen thermal gradients, and self-weight.

The shell model accurately predicted both longitudinal and circumferential stresses due to pressure loading. The beam model similarly captured the longitudinal thermal stress caused by the vertical temperature gradient and correctly estimated the effect of gravity, although gravitational stresses were found to be negligible relative to those from pressure and thermal effects. Conversely, the 2D thermoelasticity model proved unsuitable for predicting circumferential thermal stress in this configuration.

The coupled analytical formulation, combining only the pressure shell and thermal beam models, successfully reproduced the stress distribution and peak values within margins acceptable for preliminary design. At the cylinder mid-span, the analytical von Mises stress differed by only 1% from FEA, while conservatively overestimating stresses at the weld seams. This boundary overprediction is attributed to the exclusion of torispherical cap elasticity, which locally stiffened the analytical model.

Overall, this study demonstrates that classical shell and beam theory can provide fast and sufficiently accurate stress predictions in early-stage design, while also identifying regions where higher-fidelity simulation remains necessary.

List of Figures

2.1 2.2	Main components of cryogenic vessels [1]	3
2.3	Ma et al [2]	6
2.4	Adapted from Zhu et al [3]	9
3.1 3.2	Geometrical parameters of torispherical end cap	15
3.3	pending on the effect being analyzed	16
3.4	the tank	18 19
4.1	Sketches of the analytical models. a) Complete tank geometry. b) Effect of internal pressure (Model for both longitudinal and circumferential stress). c) Effect of temperature (Circumferential stress). e) Effect of gravity	21
5.1 5.2	Selected symmetry plane in order to reduce mesh size	31
6.1	Python interactive 3D plot of stress at nodes	34
6.2	Radial displacement u_r due to internal pressure: analytical solution and	
6.3	finite-element models with compliant and rigid torispherical heads Longitudinal stress σ_{zz} along the cylinder under internal pressure. (a) Global distribution showing both analytical and finite-element results. (b)	36
6.4	Enlarged view of the boundary	37
	Enlarged view of the boundary	38

6.5	Shear stress τ_{zr} along the cylinder under internal pressure. (a) Global distribution showing both analytical and finite-element results. (b) Enlarged	
	view of the boundary	39
6.6	Vertical displacement u_y under thermal loading: finite-element results with a) normally stiff and b) rigid heads compared with clamped-simply-supported (C-SS) and simply-supported-simply-supported (SS-SS) analytical beam	
	models. The undeformed outline is shown in black; deformations are mag-	
	nified 20 for clarity	41
6.7	Numerical longitudinal stress σ_{zz} under step-wise thermal gradient (tank	
	with normally stiff heads)	42
6.8	Longitudinal stress σ_{zz} as a function of the height for numerical 2m and	
	10m tanks, and analytical model. Stress at the midspan $z=1000$ mm	43
6.9	Vertical displacement field u_y for a 10 m-long cylinder under the same	
	thermal loading	44
6.10	Analytical circumferential stress $\sigma_{\varphi\varphi}$ for temperature profile A	45
6.11	Numerical circumferential stress $\sigma_{\varphi\varphi}$ for temperature profile A. Left: 2 m	
	cylinder. Right: 10 m cylinder	45
6.12	Analytical circumferential stress $\sigma_{\varphi\varphi}$ for temperature profile B	46
6.13	Numerical circumferential stress $\sigma_{\varphi\varphi}$ for temperature profile B: Left: 2 m	
	cylinder. Right: 10 m cylinder	47
6.14	Normal stress σ_{zz} due to effect of gravity: Numerical Model	48
6.15	Normal stress σ_{zz} due to effect of gravity: Analytical Model	48
6.16	Von Mises stress σ_{VM} due to combined pressure and thermal loading: com-	
	plete numerical model	50
6.17	Von Mises stress σ_{VM} due to combined pressure and thermal loading: ana-	
	lytical model	50
6.18	von Mises stress σ_{VM} for combined loading at the midspan: numerical and	
	analytical model	51

List of Tables

3.1	Geometrical parameters of the cylindrical shell and torispherical end-caps.	15
3.2	Material, fluid, and operating parameters used in the analytical model	17
6.1	Summary of analytical models and quantities for comparison with FEA	
	results	34
6.2	Comparison between FEA and analytical results at midspan-midheight and	
	at maximum locations (all values in MPa)	52

List of Symbols

Symbol Description Unit			
	Geometry		
L	Length of cylindrical shell	m	
R_o	Outer radius of shell	m	
D_o	Outer diameter of shell	m	
R_i	Inner radius of shell	m	
R_m	Mean radius $\frac{1}{2}(R_o + R_i)$	m	
h	Wall thickness	m	
DH	Dished height of torispherical cap	m	
SF	Straight-flange height of cap	m	
KR	Knuckle radius of cap	m	
CR	Crown radius of cap	m	
H	Generic liquid height in tank	m	
H_{fs}	Free-surface height	m	
A_{solid}	Area of steel wall (annulus)	m^2	
$A_{ m fluid}$	Area of fluid segment	m^2	
I	Second moment of area	m^4	
	Material and fluid properties		
E	Youngs modulus (SS 316L)	Pa	
ν	Poissons ratio (SS 316L)		
α	Linear thermal-expansion coefficient	1/K	
$ ho_{ m steel}$	Density of stainless steel	${\rm kg~m^{-3}}$	
$ ho_{ m LN2}$	Density of liquid nitrogen	${\rm kg~m^{-3}}$	
$ ho_{ m artificial}$	Artificial density used for simulation purposes	${\rm kg~m^{-3}}$	
g	Gravitational acceleration	${ m m~s^{-2}}$	
T	Temperature (generic)	K	
$T_{\rm ref}$	Reference (room) temperature	K	
$T_{\rm air}$	Ambient-air temperature	K	
$T_{ m LN2}$	Saturation temperature of LN_2	K	
ΔT	Temperature change $T_{\text{ref}} - T(y)$	K	

	Stress Representation	
σ_{ij}	Cauchy normal-stress component	Pa
$ au_{ij}$	Cauchy shear-stress component	Pa
$\sigma_1, \sigma_2, \sigma_3$	Principal stresses	Pa
I_1, I_2, I_3	Stress tensor invariants	Pa, Pa ² , Pa ³
J_2	2 nd invariant of deviatoric stress	Pa^2
k	von Mises constant = $\sigma_0/\sqrt{3}$	Pa
σ_0	yield stress in uniaxial tension	Pa
σ_{VM}	von Mises equivalent yield stress	Pa
	Shell Model	
φ	Circumferential direction (Cylindrical Coordinate)	
r	Radial direction (Cylindrical Coordinate)	
z	Longitudinal direction (Cylindrical Coordinate)	
u	Displacement	m
A	Membrane rigidity $Eh/(1-\nu^2)$	${ m N~m^{-1}}$
D	Bending rigidity $Eh^3/[12(1-\nu^2)]$	N m
N	Membrane force per length	${\rm N~m^{-1}}$
M	Bending moment per length	${ m N~m~m^{-1}}$
ζ	Through-thickness coordinate $(-h/2 \dots h/2)$	m
b	Distributed force	Pa
P	Internal pressure (generic)	Pa
	$Beam\ model$	
\overline{x}	Horizontal direction (Cartesian Coordinates)	
y	Vertical direction (Cartesian Coordinates)	
z	Longitudinal direction (Cartesian Coordinates)	
ε	Axial strain (generic)	
ε_0	Axial strain at neutral plane	
κ_0	curvature (generic)	m^{-1}
κ	curvature due to unconstrained thermal deformation	m^{-1}
w	Vertical Displacement	m
	2D Thermoelasticity model	
K, K_{φ}	Axisymmetric / first-harmonic temp. coeffs.	K
•	D_n Fourier coefficients (temperature field)	K

Contents

A	cknov	wledgments	i
K	urzfa	ssung	ii
\mathbf{A}	bstra	ct	iii
\mathbf{Li}	st of	Figures	iv
Li	${f st}$ of	Tables	v
Li	st of	symbols	vii
1	Intr	roduction	1
2	Stat	te of the art	2
	2.1	Hydrogen in Aircraft Transportation	2
	2.2	Basics of Cryogenic Vessels	3
		2.2.1 Inner Vessel Design	4
	2.3	Cooling Down Procedure	4
		2.3.1 Three-Step Cooling Down Procedure	5
		2.3.2 Temperature stratification during cooldown	5
	2.4	Previous studies on thermomechanical stresses on cylindrical tanks	6
	2.5	Solid Mechanics	8
		2.5.1 Coordinate Systems	8
		2.5.2 Stress representation	9
		2.5.3 Constitutive Relations for Solids with Thermal Loading	11
3		del Setup	14
	3.1	Complete and Simplified Geometries	15
	3.2	Material Properties	17
	3.3	Temperature Distribution	18
		3.3.1 Temperature Distribution A	18
		3.3.2 Temperature Distribution B	19
4		alytical model	20
	4.1	Effect of Internal Pressure	22
	4.2	Effect of Temperature Gradient	24
		4.2.1 Longitudinal Stress	24

		4.2.2	Circumferential Stress	
	4.3	Effect	of Gravity	28
5	Fini	ite-Elei	ment Analysis (FEA)	30
	5.1	Solver		30
	5.2	Elemer	nt formulation	30
	5.3	Mesh .		31
	5.4	Bound	ary conditions	31
	5.5	Loadin	ng scenarios	32
		5.5.1	Pressure	32
		5.5.2	Thermal	32
		5.5.3	Gravity	33
6	Res	ults: C	Comparison of Analytical and Numerical Models	34
	6.1		re	36
	0.1	i ressu	15	90
	0.1	6.1.1	Longitudinal Stress	37
	0.1			37
	0.1	6.1.1	Longitudinal Stress	37
	6.2	6.1.1 6.1.2	Longitudinal Stress	37 38
		6.1.1 6.1.2 6.1.3	Longitudinal Stress	37 38 39
		6.1.1 6.1.2 6.1.3 Therm	Longitudinal Stress	37 38 39 40
		6.1.1 6.1.2 6.1.3 Therm 6.2.1	Longitudinal Stress	37 38 39 40 40
		6.1.1 6.1.2 6.1.3 Therm 6.2.1 6.2.2 6.2.3	Longitudinal Stress	37 38 39 40 40 44
	6.2	6.1.1 6.1.2 6.1.3 Therm 6.2.1 6.2.2 6.2.3	Longitudinal Stress Circumferential Stress Stress Tensor al Longitudinal Stress Circumferential Stress Stress Tensor	37 38 39 40 40 44 47
	6.2	6.1.1 6.1.2 6.1.3 Therm 6.2.1 6.2.2 6.2.3 Gravity 6.3.1	Longitudinal Stress Circumferential Stress Stress Tensor al Longitudinal Stress Circumferential Stress Stress Tensor Stress Tensor Stress Tensor	37 38 39 40 40 44 47 47
	6.2	6.1.1 6.1.2 6.1.3 Therm 6.2.1 6.2.2 6.2.3 Gravit 6.3.1 Superi	Longitudinal Stress Circumferential Stress Stress Tensor al Longitudinal Stress Circumferential Stress Stress Tensor	37 38 39 40 40 44 47 47 48 49

1. Introduction

Commercial aviation must reduce its climate impact, and liquid hydrogen (LH₂) has emerged as a leading candidate fuel for achieving net-zero flight. Storing LH₂ at cryogenic temperatures, however, places severe thermal and mechanical demands on the tank's wall during ground operations such as cooldown and refuelling. A detailed understanding of these coupled loads is essential for safe and efficient infrastructure.

This thesis examines the demonstrator vessel of the EU project ALRIGH2T, which is developing and testing LH₂ refuelling procedures under real airport conditions [4]. The Austrian Institute of Technology (AIT) contributes high-fidelity simulations and digital-twin tools. While finite-element analysis (FEA) offers accurate predictions, it is computationally expensive when many design iterations are required. Reduced-order analytical models, carefully validated, can bridge this gap by delivering quick estimates and physical insight.

The work therefore pursues two main goals: (i) to derive a closed-form analytical model for the thermo-structural response of a horizontally mounted cryogenic tank during liquidnitrogen cooldown, and (ii) to assess its predictive capability against detailed FEA in order to identify the boundaries of applicability of classical structural mechanics methods to such problems. The guiding research question is:

Can analytical models predict the spatial variation and peak stress values that develop during the cooldown of cryogenic tanks with sufficient accuracy for preliminary design purposes?

The study is confined to a stainless-steel 316L cylinder with torispherical heads. It assumes linear-elastic, isotropic material behaviour; internal pressure; vertical temperature stratification representative of the cooldown phase; and quasi-static loading. Dynamic sloshing, cyclic fatigue, and in-flight temperature cycles lie outside the present scope.

The thesis is structured as follows. Chapter 2 reviews hydrogen aviation, cryogenic vessel technology, and prior thermal-stress research. Chapter 3 defines the tank geometry, material data, and idealised temperature fields. Chapter 4 develops the analytical solution for pressure, temperature, and gravity loads. Chapter 5 presents the finite-element model used for validation. Chapter 6 compares the analytical and numerical results and discusses the findings. Chapter 7 summarises the conclusions and outlines avenues for future work.

2. State of the art

2.1 Hydrogen in Aircraft Transportation

The transition to carbon-neutral energy systems is no longer a long term aspiration but an immediate engineering mandate. Fossil derived hydrocarbons cannot be burned at today's scale without exceeding the CO_2 budget compatible with a stable climate, so the next energy infrastructure must rely on resources that are effectively inexhaustible (solar, wind, nuclear), free of greenhouse-gas emissions, and universally accessible [5]. Energy carriers with these attributes must also be storable and deployable in every sector, specially in aviation, whose contribution to global warming is growing faster than most others [5].

Hydrogen fulfills these systemic requirements better than any other known fuel. When produced by splitting water with renewable electricity, it forms a closed, carbon-free cycle of $H_2 \leftrightarrow H_2O$ and can be generated wherever water and power are available. Liquid hydrogen (LH₂) packs the highest gravimetric energy density of any practical fuel [6], so in principle, an aircraft can fly farther or carry more payload without increasing take-off mass. Moreover, the cryogenic temperature of LH₂ makes it an excellent coolant for engines, power electronics, and high-temperature superconducting drives now under study [6].

For aviation the storage medium is decisive. Among the physical options (compressed gas, cryogenic liquid, and cryo-compressed gas) only LH₂ provides a volumetric density low enough to keep tank size acceptable while avoiding the very high wall stresses that accompany 350-700 bar compressed gas systems [7]. At 20K the density of LH₂ (\approx 71 kg m⁻³) is roughly five-and-a-half times that of 164-bar gaseous hydrogen at ambient temperature, and achieving comparable densities with warm gas would drive vessel masses and costs far beyond what aircraft can tolerate [8].

However, hydrogen's physical properties also impose the main technical barriers. Its low critical temperature demands vessels that combine high mechanical strength with effective thermal insulation [9]. Unlike an ideal gas, H₂ becomes increasingly non-ideal above ∼150bar, so volumetric efficiency rises slowly with pressure while the structural penalty rises quickly [10]. Repeated pressure cycling stresses liners and requires rigorous certification under ISO, CGA, and ASME codes, hindering any mass advantage [10]. On top of that, LH₂ has an exceptionally small enthalpy of vaporisation of 0.46 kJmol⁻¹ [9]. Consequently, even small heat leaks drive boil-off. Practical tanks therefore use double-walled, vacuum-jacketed stainless-steel or aluminium vessels wrapped with multilayer insulation (MLI) films to cut conduction, convection, and radiation to the lowest possible levels [9]. Venting strategies or re-liquefaction loops are required to handle the inevitable boil-off

during ground operations and extended loiter [9].

The research frontier therefore centres on the thermomechanical behaviour of lightweight, vacuum-insulated LH₂ tanks under realistic mission profiles: rapid filling, climb-cruise thermal soak, vibration, slosh, and repeated pressure-temperature cycling over decades [11]. Material compatibility with hydrogen embrittlement, insulation durability, and integrated heat-exchanger concepts remain partially resolved [11]. A deeper understanding of these coupled thermal and mechanical loads is essential before regulatory authorities will certify large-scale hydrogen aircraft [11].

2.2 Basics of Cryogenic Vessels

High-performance cryogenic storage vessels are typically based on a double-walled design, where the space between the inner and outer vessels is filled with insulation material and evacuated to create a vacuum [1]. The key components of such vessels are illustrated in Figure 2.1. The inner vessel, also referred to as the product container, holds the cryogenic fluid. This is surrounded by an outer vessel, or vacuum jacket, which maintains the vacuum necessary for the insulation to function effectively and acts as a vapor barrier. In the case of liquid hydrogen, it prevents the ingress of air or moisture into the cold inner container [1].

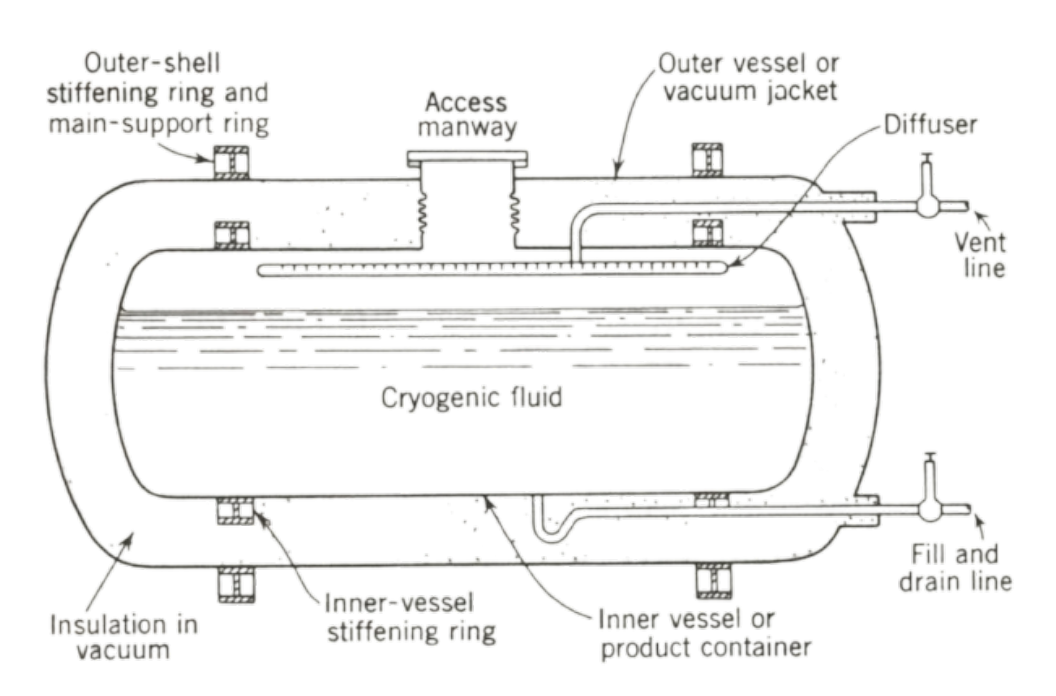


Figure 2.1: Main components of cryogenic vessels [1]

The space between the two vessels is crucial for thermal insulation. For large-scale storage systems, separate fill and drain lines are typically included. A vapor vent line is also essential to release vapor generated by unavoidable heat inleak. Additionally, a mechanism must be provided to extract the liquid from the container, which is commonly achieved either through pressurization of the inner vessel or by using a cryogenic liquid pump [12]. When pressurization is employed, a vapor diffuser is installed in the vent line to ensure

even distribution of the warm pressurizing gas throughout the ullage space (the vapor space above the liquid level).

Cryogenic vessels are intentionally not filled to full capacity. This is due to the continuous heat inleak into the product container, which causes vaporization of the liquid. Without sufficient ullage space, internal pressure could rise rapidly. Moreover, inadequate precooling of the inner vessel during rapid filling can result in excessive boil-off. In such cases, liquid could be expelled through the vent tube if no ullage space is provided [13]. A typical design includes approximately 10% ullage volume to mitigate these issues [14].

Cryogenic storage vessels can be fabricated in a variety of geometries, including cylindrical, spherical, and conical shapes. Among these, cylindrical vessels with torispherical, elliptical, or hemispherical end caps are considered to be among the most economical and structurally efficient configurations [7].

2.2.1 Inner Vessel Design

The product container must withstand the design internal pressure, the weight of the fluid within the vessel and the thermomechanical loading due to temperature differences [1][13]. The inner vessel must be fabricated from materials that are compatible with the cryogenic fluid. Consequently, stainless steel, aluminum, Monel, and occasionally copper are commonly selected for the inner shell [1]. These materials are significantly more expensive than conventional carbon steel, prompting designers to minimize the wall thickness of the inner vessel to control costs. Furthermore, a thick-walled vessel has several drawbacks, it takes longer to cool down, results in greater cryogen loss during the cooldown process, and increases the likelihood of developing thermal stresses within the vessel wall [1].

The details of cryogenic-fluid-storage design are covered in such standards as the ASME Boiler and Pressure Vessel Code Section VIII [15] or the ISO 20421-1:2019 [16]. Due to the high density of the tank wall material, the required wall thickness is typically determined in accordance with established design standards. For cylindrical shells, the ASME Boiler and Pressure Vessel Code Section VIII provides the following formula for calculating the minimum required wall thickness:

$$t = \frac{PR_i}{S\mathcal{E} - 0.6P} , \qquad (2.1)$$

where P is the internal pressure, R_i is the inside radius of the shell, S is the maximum allowable stress value and \mathcal{E} is a factor called joint efficiency. Values for S and \mathcal{E} for different materials and joints are proposed as well in the code. There also exist more detailed formulas in different standards [7], but they usually rely on the Maximum Allowable Working Pressure (MAWP), which typically ranges from 1.60 to 2.15 MPa for cryogenic filling procedures [17].

2.3 Cooling Down Procedure

The cooldown of cryogenic hydrogen tanks prior to liquid hydrogen (LH₂) refuelling is a critical operation designed to reduce thermal stresses and ensure the structural integrity of the system. This stepwise thermal conditioning process is widely practiced in the industry and currently being standardized at the international level [18]. Specifications for LH₂ fuelling and hardware interfaces, developed under the Clean Energy Partnership (CEP) and finalized in 2022, are undergoing ISO standardization [19]. Detailed process characteristics are also described in technical literature [17] and manufacturer procedures [18].

2.3.1 Three-Step Cooling Down Procedure

The cooling down of the tank is typically performed using liquid nitrogen (LN₂), which has a boiling point of approximately 80K. It serves as an intermediate cooling agent prior to LH₂ (20K), helping to reduce the risk of thermal shock and excessive material contraction. The LN₂ cooling process is generally divided into three main steps [17]¹.

The first step is the initial LN_2 filling, during which LN_2 is introduced into the tank at a controlled rate of around 400 kg/h. The process continues until the LN_2 level reaches approximately 50% of the tank's internal volume. This initiates a gradual reduction of temperature across the inner vessel walls and associated piping.

Following the initial fill, the system enters the temperature equalization phase. Once the fill volume is reached, the system holds for approximately one hour. During this period, LN_2 remains inside the tank and continues absorbing heat from the structure. This step ensures that the internal surfaces of the tank reach a uniform cryogenic temperature close to that of LN_2 . At the end of this phase, the internal pressure of the tank typically reaches 1.6 MPa, consistent with standard operating conditions. Cryogenic tanks are also equipped with pressure relief devices to protect against over-pressurization. These valves are typically set to activate below the maximum allowable working pressure, which is generally $\approx 2.0 \, \text{MPa}$ for LH_2 storage systems.

Finally, in the LN_2 purging phase, after thermal equilibrium is established, the LN_2 is purged from the tank using gaseous nitrogen or controlled depressurization. This step removes any residual liquid, ensuring the system is cold and clean in preparation for the subsequent LH_2 fuelling process.

2.3.2 Temperature stratification during cooldown

Numerical and experimental studies have shown that the cooldown and refuelling processes create a vertical temperature stratification inside the tank [2][20][21]. At the beginning of the process, the incoming cryogenic liquid falls to the bottom of the tank, and no clear liquid-gas interface is formed. When the cold liquid contacts the warmer tank walls, rapid evaporation occurs. The resulting cold vapor rises and cools the ullage region, creating a temperature drop and forming a vertical temperature gradient, as shown in Figure 2.2. Although the example focuses on a vertical tank, research indicates that a similar pattern is observed in the vertical direction of horizontal tanks [22].

As more liquid collects at the bottom due to gravity, a stable liquid surface is gradually established. The liquid level continues to rise and becomes more stable over time as

 $^{^{1}}$ The procedure is standardized for the liquid nitrogen refuelling but also employed during the LN₂ cooling down phase.

filling progresses [20]. The ullage region maintains a vertical temperature stratification throughout the process, with the lowest temperatures near the liquid surface and the highest at the top of the tank [20].

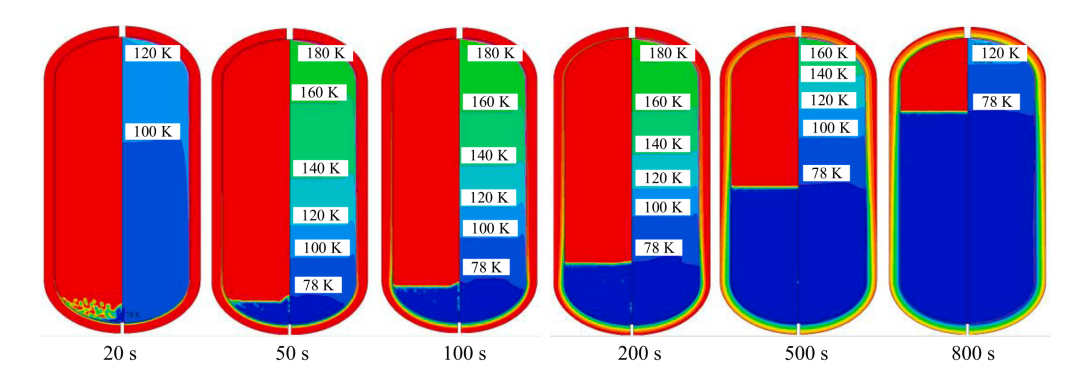


Figure 2.2: Graphic contours of phase distribution (left half of the tank) and temperature field (right half of the tank) in LN2 tank during filling. Adopted from Ma et al [2].

Experimental observations in horizontal tanks indicate that appreciable temperature gradients occur solely in the vertical direction. With a well-designed cooling system the longitudinal gradient along the tank axis is negligible, so the temperature can be treated as uniform over any cross-section normal to the axis [22].

2.4 Previous studies on thermomechanical stresses on cylindrical tanks

The structural response of cryogenic storage vessels is governed by three principal load cases: self-weight, internal pressure, and temperature-induced stresses during cooldown. Classical elasticity already provides closed-form descriptions of each. As described in Timoshenko's historical review [23], self-weight bending was treated by Jacob Bernoulli and generalised by Euler, formalised for engineering design by Navier and Saint-Venant, and codified in the hand-calculation formulas gathered by Timoshenko [24].

The pressure problem followed a parallel trajectory. The Young-Laplace relation (1806) revealed the 2:1 hoop-to-longitudinal stress ratio for thin tubes; Fairbairn and Hodgkinson confirmed it experimentally, Lamé extended it to thick cylinders, and Love, Flügge, and Donnell embedded these results in shell theory. The work of Timoshenko and Woinowsky-Krieger remains the canonical synthesis for modern pressure-vessel design [25].

Cooldown introduces a third, often critical, load. During initial filling with liquid nitrogen, forced-convection boiling on the hot inner wall creates steep, transient temperature gradients that superpose membrane and bending stresses [26]. Because the boundary conditions vary in space and time, analytical heat-transfer solutions are feasible only for idealised geometries; complex tanks therefore rely on coupled numerical-analytical techniques [27]. Historical reviews [28][29] state how the theoretical basis was laid by Duhamel and Love, extended to beams and plates by Timoshenko, Biot and Boley, and adapted to cylindrical shells by Goodier, Flügge and Donnell. Boley's energy methods still provide

rigorous bounds for thin-walled members [30][31]. Kent's thin-wall solution for axial and radial gradients [32] was generalised circumferentially by Goodier [33] and compacted by Sauer for thermally stratified pipes [34].

Regarding recent work, a fully three-dimensional description was introduced by Irfan [35], who characterised thermal stresses in radiant tubes arising from simultaneous axial, circumferential, and radial temperature gradients, and validated the results against finite-element computations. Building on the two-dimensional thermo-elasticity formulations of Timoshenko [24], Boley [30], and Hetnarski [31], Logie [36] proposed an efficient semi-analytical procedure for thin solar-receiver tubes exposed to strongly non-axisymmetric heat fluxes. Their approach retains the speed of closed-form expressions while capturing the essential coupling between temperature and stress fields. To remove any geometric idealisation, Montoya [37] developed a full three-dimensional finite-element model that incorporates realistic mechanical boundary conditions and allows radial, circumferential, and axial temperature variations to be analysed separately. Comparison with the classical two-dimensional solutions confirmed the accuracy of the numerical model and highlighted the relative influence of each temperature gradient on the peak stress distribution.

On the numerical aspect, Ma [2] conducted a comprehensive study on the chill-down behavior of aluminum vertical tanks filled with liquid nitrogen. The investigation emphasized how non-uniform cooling, driven by cryogenic fluid injection, initiates thermal deformation due to rapid temperature shifts across the tank wall. Ma identified key factors influencing the filling process: liquid injection method, initial wall temperature, inlet liquid temperature, and flowrate. An analytical model incorporating CFD-derived wall temperature distributions was used to predict thermal stress evolution. Notably, the tank wall exhibited a shrinkage pattern in both radial and longitudinal directions as the liquid level rose, with maximum deformation localized at the top of the tank due to the fixed boundary at the base.

Thermal stress analysis revealed that radial stress remained negligible (around 0.1 MPa) due to minimal radial temperature and pressure gradients, indicating a predominantly planar stress state. However, longitudinal stress dominated over circumferential stress because the temperature was more uniform circumferentially. A notable peak-trough behavior in longitudinal thermal stress near the liquid surface was attributed to the differential cooling rates between submerged and unsubmerged wall sections. As seen in Figure 2.3 upon submersion, the wall experienced a transition from tensile to compressive stress, correlating closely with the rise of the liquid level; an insight supported by comparisons with CFD simulations [2].

Complementing Ma's findings, Xia [22] explored the chill-down of a 60 m³ horizontal storage tank using both experimental and numerical approaches. A finite element model was developed, with assumptions including adiabatic outer boundaries and neglecting the insulation layer, justified by its minimal thermal role during rapid chill-down. The simulation onset corresponded with the first appearance of liquid at the tank's bottom, where liquid nitrogen gradually accumulated due to gravity-dominated flow behavior. Xia observed that, in horizontal tanks, circumferential stress prevailed below the liquid level once a stable stratified layer formed. Additionally, thermal stress distribution was found to correlate directly with the temperature gradient and structural constraints, especially at fixed boundaries where local stress concentrations could develop.

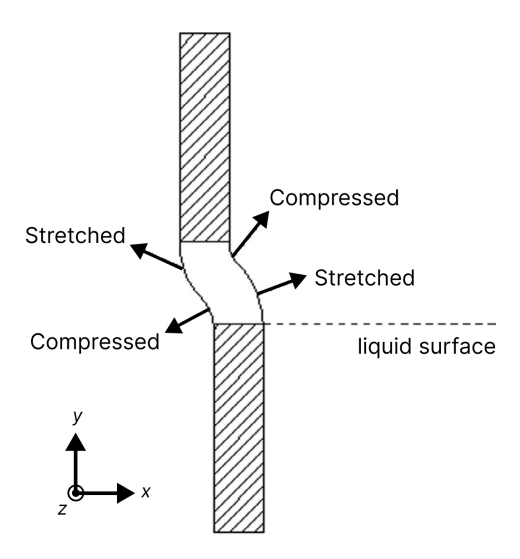


Figure 2.3: The deformation and stress state of the tank's wall near the liquid surface. Adapted from Zhu et al [3].

Both studies converge on the critical role of temperature gradients and boundary constraints in dictating thermal stress patterns. While Ma [2] highlights the vertical tank's susceptibility to longitudinal stresses due to uneven chill-down above and below the liquid line, Xia [22] shows that in horizontal tanks, stress localization is driven by circumferential constraints and bottom-layer accumulation. The studies reinforce the importance of filling method design and thermal management to minimize stress-induced failure risks in cryogenic tanks.

2.5 Solid Mechanics

2.5.1 Coordinate Systems

Two right-handed reference frames are employed throughout this thesis. The adopted frame is stated at the start of every model.

Cartesian frame.

Figure 2.4(a) shows the global Cartesian (x, y, z) frame. The z-axis coincides with the longitudinal centre-line of the tank; the cross-sectional plane is therefore the x-y plane. The vertical axis y is taken positive upward (opposite to gravity) and the horizontal axis x completes the right-handed triad.

Cylindrical frame

The cylindrical (φ, r, z) frame, shown in Fig. 2.4(b), shares the longitudinal coordinate z. The radial coordinate r is measured inwards from the z-axis, and the azimuthal coordinate φ (positive counter-clockwise when viewed from the positive z side) specifies the circumferential position. Using both frames allows stresses and boundary conditions to be expressed in the most convenient form for each loading scenario.

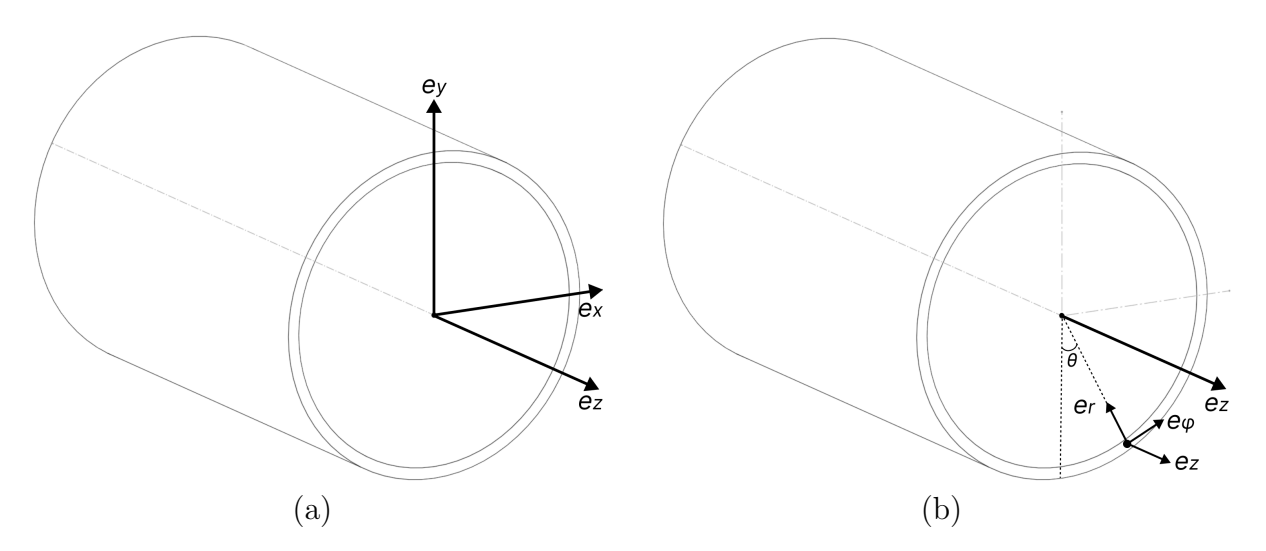


Figure 2.4: Coordinate systems adopted in this work: (a) Cartesian (x, y, z) frame with z along the tank axis, (b) cylindrical (φ, r, z) frame sharing the same z axis.

2.5.2 Stress representation

Cauchy stress tensor

At every material point the state of stress is completely described by the second-order Cauchy stress tensor. In cartesian coordinates, the components are given by

$$\boldsymbol{\sigma} = \begin{bmatrix} \sigma_{xx} & \tau_{xy} & \tau_{xz} \\ \tau_{yx} & \sigma_{yy} & \tau_{yz} \\ \tau_{zx} & \tau_{zy} & \sigma_{zz} \end{bmatrix} . \tag{2.2}$$

For thin cylindrical shells the natural basis is $\{\mathbf{e}_{\varphi}, \mathbf{e}_r, \mathbf{e}_z\}$, and the components of the stress tensor are

$$\boldsymbol{\sigma} = \begin{bmatrix} \sigma_{\varphi\varphi} & \tau_{\varphi r} & \tau_{\varphi z} \\ \tau_{r\varphi} & \sigma_{rr} & \tau_{rz} \\ \tau_{z\varphi} & \tau_{zr} & \sigma_{zz} \end{bmatrix} . \tag{2.3}$$

The normal components have the conventional names σ_{rr} (radial), $\sigma_{\varphi\varphi}$ (hoop or circumferential), and σ_{zz} (axial or longitudinal).

Principal Stresses

It is always possible to find a set of axes (1, 2, 3) along which the shear stress components vanish. In this case, the normal stresses, σ_1 , σ_2 , and σ_3 , are called *principal stresses*, and the 1, 2, and 3 axes are the *principal stress axes* [38]. The magnitudes of the principal stresses, σ_p , are the three roots of

$$\sigma_p^3 - I_1 \sigma_p^2 - I_2 \sigma_p - I_3 = 0, (2.4)$$

where

$$I_{1} = \sigma_{xx} + \sigma_{yy} + \sigma_{zz},$$

$$I_{2} = \tau_{yz}^{2} + \tau_{zx}^{2} + \tau_{xy}^{2} - \sigma_{yy}\sigma_{zz} - \sigma_{zz}\sigma_{xx} - \sigma_{xx}\sigma_{yy},$$

$$I_{3} = \sigma_{xx}\sigma_{yy}\sigma_{zz} + 2\tau_{yz}\tau_{zx}\tau_{xy} - \sigma_{xx}\tau_{yz}^{2} - \sigma_{yy}\tau_{zx}^{2} - \sigma_{zz}\tau_{xy}^{2}.$$

$$(2.5)$$

The first invariant, $I_1 = -3p$, where p is the pressure. I_1 , I_2 , and I_3 are independent of the orientation of the axes and are therefore called *stress invariants* [38]. In terms of the principal stresses, the invariants are

$$I_1 = \sigma_1 + \sigma_2 + \sigma_3,$$

$$I_2 = -\sigma_2 \sigma_3 - \sigma_3 \sigma_1 - \sigma_1 \sigma_2,$$

$$I_3 = \sigma_1 \sigma_2 \sigma_3.$$
(2.6)

Von Mises (Distortion-Energy) Yield Criterion for Isotropic Ductile Metals

In uniaxial tension tests macroscopic plastic flow begins when the applied normal stress reaches the uniaxial yield value σ_0 . For more complex loading the onset of yielding is correlated with an invariant measure of the stress state rather than with any single stress component [39]. Von Mises (1913) observed that pure hydrostatic pressure, which merely changes volume, does not provoke yielding in a continuous ductile solid, whereas shape-changing (deviatoric) stresses do. Consequently the yield condition must depend only on the stress deviator and must be independent of the orientation of the axes, i.e. it must be formulated in terms of tensor invariants. He proposed that yielding occurs when the second invariant of the stress deviator, J_2 , reaches a critical value k^2

$$J_2 = k^2, J_2 = \frac{1}{6} \Big[(\sigma_1 - \sigma_2)^2 + (\sigma_2 - \sigma_3)^2 + (\sigma_3 - \sigma_1)^2 \Big]. (2.7)$$

Calibrating the constant k with the uniaxial tension test, where $\sigma_1 = \sigma_0$ and $\sigma_2 = \sigma_3 = 0$, gives

$$\sigma_0 = \sqrt{3} k. \tag{2.8}$$

Substitution yields the classical von Mises (or distortion-energy) criterion expressed in principal stresses,

$$\sigma_{VM} = \frac{1}{\sqrt{2}} \left[(\sigma_1 - \sigma_2)^2 + (\sigma_2 - \sigma_3)^2 + (\sigma_3 - \sigma_1)^2 \right]^{1/2}, \tag{2.9}$$

and, in Cartesian components,

$$\sigma_{VM} = \frac{1}{\sqrt{2}} \left[(\sigma_x - \sigma_y)^2 + (\sigma_y - \sigma_z)^2 + (\sigma_z - \sigma_x)^2 + 6\left(\tau_{xy}^2 + \tau_{yz}^2 + \tau_{xz}^2\right) \right]^{1/2}.$$
 (2.10)

Because the criterion depends only on stress differences, the hydrostatic component is absent, rendering the relation invariant under pressure and fully compatible with the empirical fact that metals do not yield under uniform compression alone [39]. The squared-difference form also eliminates any dependence on the sign of individual stresses, making the relation convenient when the ordering of principal stresses is unknown.

Hencky (1924) later showed that this formulation is equivalent to requiring the specific distortion (shear) energy to reach a critical value, thereby giving the criterion a clear

physical interpretation: yielding begins when the energy associated with change of shape, as distinct from change of volume, attains the value measured in a uniaxial test [39]. Owing to its coordinate invariance, insensitivity to hydrostatic stress and excellent correlation with multiaxial experimental data, the von Mises criterion is widely accepted for predicting the onset of plastic flow in isotropic, ductile metals such as structural steels [39].

2.5.3 Constitutive Relations for Solids with Thermal Loading

Constitutive equations in solid mechanics maintain the same fundamental form regardless of the coordinate system used, including Cartesian and cylindrical coordinates [40]. This invariance arises from the principle of coordinate frame indifference, which requires that material response laws remain unchanged under coordinate transformations. While tensor components (e.g., stress or strain) must be expressed in the basis vectors of the chosen coordinate system, the underlying physical relationships between these quantities retain identical structure [40].

Three dimensional body

In three dimensions, the generalized Hooke's law for a linearly elastic, isotropic material relates the stress and strain tensors through a constitutive matrix. Using matrix (Voigt) notation, the stress vector $\boldsymbol{\sigma}$ and the strain vector $\boldsymbol{\varepsilon}$ are expressed as 6×1 column vectors

$$\boldsymbol{\sigma} = \begin{bmatrix} \sigma_{xx} \\ \sigma_{yy} \\ \sigma_{zz} \\ \sigma_{yz} \\ \sigma_{xz} \\ \sigma_{xy} \end{bmatrix}, \quad \boldsymbol{\varepsilon} = \begin{bmatrix} \varepsilon_{xx} \\ \varepsilon_{yy} \\ \varepsilon_{zz} \\ \gamma_{yz} \\ \gamma_{xz} \\ \gamma_{xy} \end{bmatrix}. \tag{2.11}$$

The linear constitutive relation is then written as

$$\sigma = \mathbf{C}\,\boldsymbol{\varepsilon}\,\,\,\,(2.12)$$

where C is the 6×6 stiffness matrix for isotropic materials, defined as

$$\mathbf{C} = \frac{E}{(1+\nu)(1-2\nu)} \begin{bmatrix} 1-\nu & \nu & \nu & 0 & 0 & 0\\ \nu & 1-\nu & \nu & 0 & 0 & 0\\ \nu & \nu & 1-\nu & 0 & 0 & 0\\ 0 & 0 & 0 & \frac{1-2\nu}{2} & 0 & 0\\ 0 & 0 & 0 & 0 & \frac{1-2\nu}{2} & 0\\ 0 & 0 & 0 & 0 & 0 & \frac{1-2\nu}{2} \end{bmatrix} . \tag{2.13}$$

When thermal effects are included, the temperature change ΔT introduces an additional strain field due to uniform thermal expansion. The generalized Hooke's law then becomes

$$\sigma = \mathbf{C} \left(\varepsilon - \varepsilon^{\text{th}} \right) ,$$
 (2.14)

with the thermal strain vector defined as

$$\boldsymbol{\varepsilon}^{\text{th}} = \alpha \Delta T \begin{bmatrix} 1\\1\\1\\0\\0\\0 \end{bmatrix}. \tag{2.15}$$

Shell model

The shell model is based on the assumption that the thickness is much smaller than the in-plane dimensions, and the structure behaves primarily in a two-dimensional manner. Normals to the mid-surface are assumed to remain straight and perpendicular after deformation (Kirchhoff-Love hypothesis), and the through-thickness stress component σ_{xx} is negligible (plane stress condition) [25]. Under these assumptions, the in-plane stress vector is reduced to three components:

$$\boldsymbol{\sigma}^{\text{shell}} = \begin{bmatrix} \sigma_{zz} \\ \sigma_{yy} \\ \sigma_{zy} \end{bmatrix}, \quad \boldsymbol{\varepsilon}^{\text{shell}} = \begin{bmatrix} \varepsilon_{zz} \\ \varepsilon_{yy} \\ \gamma_{zy} \end{bmatrix} , \qquad (2.16)$$

and the constitutive relation becomes

$$\sigma^{\text{shell}} = \mathbf{C}^{\text{shell}} \left(\boldsymbol{\varepsilon}^{\text{shell}} - \boldsymbol{\varepsilon}^{\text{th}} \right) ,$$
 (2.17)

with the plane stress elasticity matrix defined as

$$\mathbf{C}^{\text{shell}} = \frac{E}{1 - \nu^2} \begin{bmatrix} 1 & \nu & 0 \\ \nu & 1 & 0 \\ 0 & 0 & \frac{1 - \nu}{2} \end{bmatrix}, \quad \boldsymbol{\varepsilon}^{\text{th}} = \frac{\alpha \Delta T}{1 - \nu} \begin{bmatrix} 1 \\ 1 \\ 0 \end{bmatrix}.$$
 (2.18)

For thin shells, the internal resultants are obtained by integrating the stress components through the thickness. Membrane forces per unit length are obtained by multiplying the stress vector by the thickness h, while bending moments involve curvature terms and a factor of h^3 , leading to similar matrix structures with scaled coefficients.

Beam model

The beam model assumes that the cross-sectional dimensions are much smaller than the length and that the structure primarily resists loads through axial and bending behavior. Plane sections remain planar and perpendicular to the neutral axis (Euler-Bernoulli hypothesis), and transverse shear strain is assumed to be zero [40]. The stress state is dominated by the axial stress σ_{zz} , which varies linearly along the height of the beam. The axial strain as a function of position y from the neutral axis is given by

$$\varepsilon_{zz}(y) = \varepsilon_0 - y\kappa$$
, (2.19)

where ε_0 is the axial strain of the neutral axis, and κ is the curvature. The axial stress becomes

$$\sigma_{zz}(y) = E\left(\varepsilon_0 - y\kappa - \alpha\Delta T\right). \tag{2.20}$$

Integrating the stress over the cross-section gives the normal force N and bending moment M, and assuming that the ΔT is constant over the thickness, the constitutive relation in matrix form becomes

$$\begin{bmatrix} N \\ M \end{bmatrix} = \begin{bmatrix} EA & 0 \\ 0 & EI \end{bmatrix} \left(\begin{bmatrix} \varepsilon_0 \\ \kappa \end{bmatrix} - \begin{bmatrix} \alpha \Delta T \\ 0 \end{bmatrix} \right) \tag{2.21}$$

where A is the cross-sectional area and I is the second moment of area. This relation expresses the beam's response to combined mechanical and thermal loading within the assumptions of linear elasticity and one-dimensional behavior.

3. Model Setup

The computer-aided design (CAD) model of the tank is based on a cryogenic pressure vessel developed by the Salzburger Aluminium Group (SAG). All non-structural components have been removed, preserving only the primary load-bearing elements: the cylindrical shell and the torispherical heads. This configuration is hereafter referred to as the Complete Geometry and will be used for finite element analysis, serving as a reference for evaluating the accuracy of the analytical models.

For analytical purposes, a simplified version of the CAD model -referred to as the Simplified Geometry- is introduced, in which the torispherical heads are omitted. This simplification is done to reduce the complexity of the closed-form analytical solutions.

For each load case, an analytical model is formulated based on the Simplified Geometry. The associated assumptions, loading conditions, and boundary conditions are detailed in Section 4.

3.1 Complete and Simplified Geometries

The Complete Geometry consists of a cylindrical circular hollow shell section welded at both ends to torispherical caps by external welds. The geometrical parameters of the tank are summarized in Table 3.1 and the parameters of the torispherical caps are illustrated in Figure 3.1. The tank's left end cap is welded to a fixed bearing that constraints any displacement and rotation. The right end cap allows movement in the longitudinal axis z and rotation in the x axis, accounting for the possible contraction of the tank during the cooldown, but constraints the rest of displacements and rotations. There are no further supports nor stiffening rings along the axial direction, so far away from the end caps, the tank is allowed to displace freely in the radial direction.

Table 3.1: Geometrical	peremeters of t	the evlindrical	aboll and t	orignhorical	and anno
Table 5.1. Geometrical	parameters or t	me cymiancai	suen and t	orisphericar	enu-caps.

Cylindrical section						
Property Symbol Value Unit						
Length of cylindrical section	L	2.000	m			
Outer radius of tank	R_o	0.330	m			
Inner radius of tank	R_i	0.325	m			
Wall thickness	h	0.005	m			
Torispherical caps						
Dished height	DH	0.170	m			
Straight flange height	SF	0.015	m			
Knuckle radius	KR	0.518	m			
Crown radius	CR	0.010	m			
Outer diameter of end-cap	D_o	0.660	m			
Wall thickness	h	0.005	m			

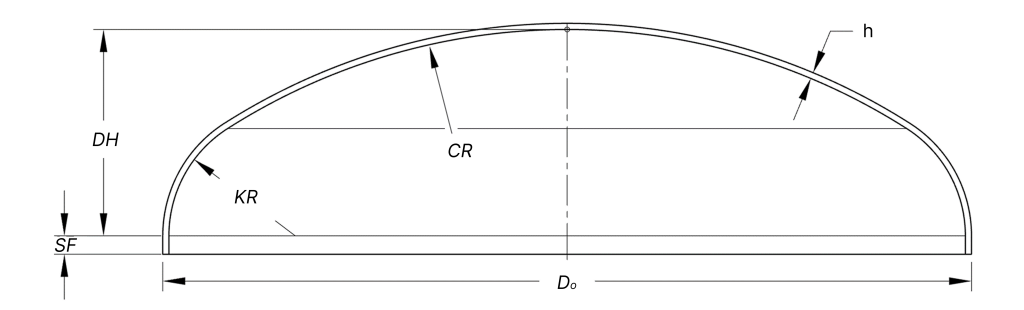


Figure 3.1: Geometrical parameters of torispherical end cap.

A comparison between the Complete Geometry and the Simplified Geometry is presented in Figure 3.2. Both geometries share identical overall dimensions, including length, radius, and wall thickness.

In the Simplified Geometry, the torispherical heads are omitted. Their structural effect is accounted for differently depending on the analytical model. In the pressure analysis, they are replaced by boundary conditions applied at the weld seam. For the gravity and thermal load cases, the cylindrical section is extended to preserve the overall span between the supported ends, as illustrated by the gray area in Figure 3.2b.

By comparing the numerical results with the analytical results, it is possible to evaluate the influence of including or excluding the torispherical caps on the thermomechanical response.

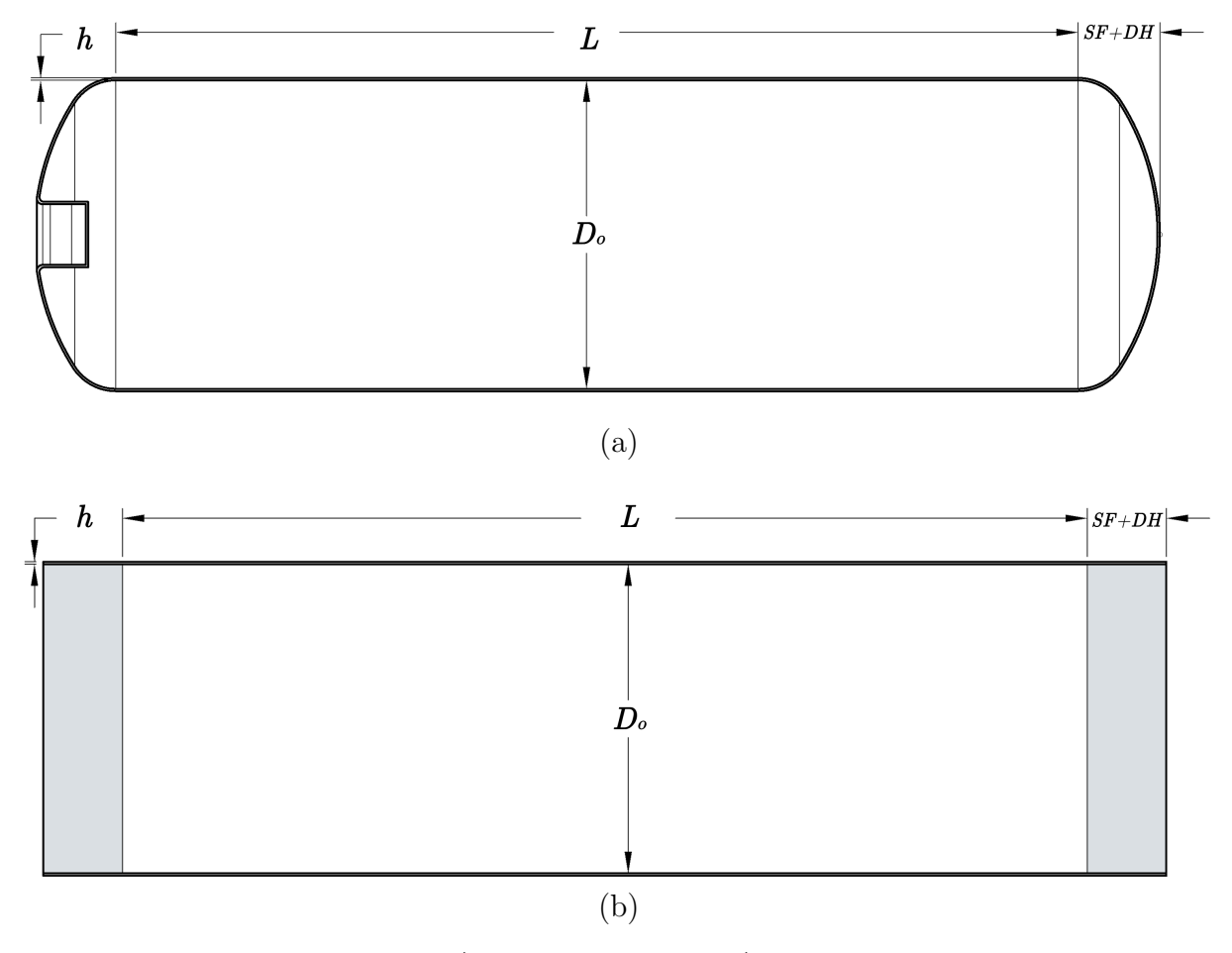


Figure 3.2: Section-view drawing of **a)** Complete Geometry **b)** Simplified Geometry. The gray area in the Simplified Geometry will be added or removed depending on the effect being analyzed.

3.2 Material Properties

The material selected for the tank is stainless steel 316L (EN 1.4404). While its mechanical and thermal properties are known to vary with temperature, for the purpose of comparing the numerical and analytical models, the material properties remain constant. The adopted values represent average properties obtained from the publicly available cryogenic materials database of the National Institue of Standards and Technology (NIST) [41]. Liquid nitrogen is used as the filling fluid. Other parameters employed in the calculations are taken from the standard cooling down-procedure (See Section 2.3) and summarized in Table 3.2.

Table 3.2: Material, fluid, and operating parameters used in the analytical model.

Material properties (SS 316L)						
Property	Symbol	Value	Unit			
Young's modulus	E	2.00×10^{11}	Pa			
Linear thermal-expansion coefficient	α	1.00×10^{-5}	K^{-1}			
Density of steel	$ ho_{ m steel}$	8.00×10^{3}	${\rm kgm^{-3}}$			
Poisson's ratio	ν	3.00×10^{-1}	_			
Fluid prop	erties					
Gas temperature	$T_{\rm air}$	3.00×10^{2}	K			
Reference temperature (room)	T_{ref}	3.00×10^2	K			
Liquid nitrogen temperature	$T_{ m LN2}$	8.00×10^{1}	K			
Liquid nitrogen density	$ ho_{ m LN2}$	8.00×10^{2}	${\rm kgm^{-3}}$			
Height of free surface	$H_{ m fs}$	3.30×10^{-1}	m			
Other parameters						
Gravitational acceleration	g	9.81	${ m ms^{-2}}$			
Maximum internal pressure	P_{\max}	2.00×10^{6}	Pa			
Tank-wall temperature ^a	T	_	_			

^a Temperature distributions are provided in Section 3.3.

Since the density of gas nitrogen is really low in comparison with the density of the liquid nitrogen, the fluid area will be defined in terms of the liquid height H. In this case, the area is defined by the circular segment

$$A_{\text{fluid}} = R_m^2 \cdot \arccos\left(\frac{R_m - H}{R_i}\right) - (R_m - H) \cdot \sqrt{(2R_m H - H^2)}, \qquad (3.1)$$

where R_m is the mean radius of the tank. The area of the solid section is defined by the area of the annular cross section, with h being the wall thickness of the tank

$$A_{solid} = \pi \left((R_m + h)^2 - (R_m - h)^2 \right). \tag{3.2}$$

3.3 Temperature Distribution

3.3.1 Temperature Distribution A

The main scenario, titled Temperature Distribution A, is depicted in Figure 3.3 and corresponds to an idealized, abrupt stratification in which one half of the tank is subjected to a cold temperature and the other half to a warm temperature. This scenario imposes a highly demanding thermal gradient, serving as a conservative approximation of the actual thermal stratification that occurs during operation.

It should be remarked that, while in reality temperature must vary continuously throughout the tank, this discontinuous temperature distribution represents a highly idealized and maybe even non-physical case. Indeed, such a discontinuity implies a derivative that is not defined in the classical sense —the heat flux being infinite at the interface and zero elsewhere— highlighting the theoretical nature of this approximation. In practice, the thermal loading is expected to be less severe, with a more gradual temperature increase from the cold bottom to the warm top of the tank. Nevertheless, this idealized case enables the evaluation of the maximum stresses predicted by both the analytical and numerical models. If the analytical model proves capable of accurately capturing the stresses under such aggressive thermal conditions, it can be considered a reliable and conservative tool for preliminary design.

$$T(y) = \begin{cases} T_{\text{LH2}}, & \text{for } y < H_{\text{fs}} \\ T_{\text{gas}}, & \text{for } y \ge H_{\text{fs}} \end{cases}, \tag{3.3}$$

where $H_{\rm fs}$ is the height of the free-surface, taken as R_m

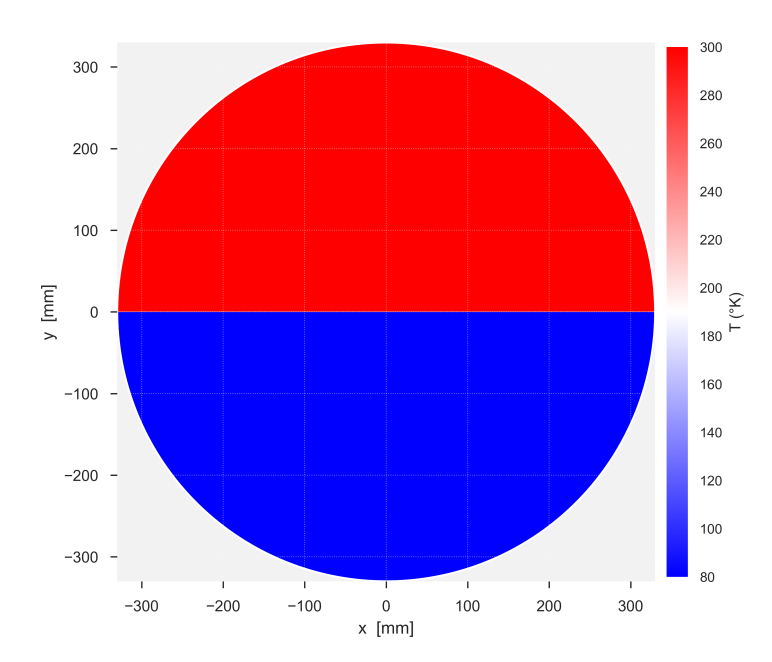


Figure 3.3: Temperature distribution A: Abrupt temperature change in the middle of the tank.

3.3.2 Temperature Distribution B

A second scenario, named Temperature Distribution B, is considered as well only for the analysis of circumferential (hoop) stresses. This distribution assumes a linear increase in temperature along the vertical direction, starting from a cold temperature at the bottom—corresponding to liquid nitrogen— and reaching room temperature at the top of the tank, as illustrated in Figure 3.4. This gradient provides a conservative approximation of the temperature distribution at the beginning of the cooldown procedure. The temperature profile is defined as

$$T(y) = T_{\text{LN}2} + (T_{\text{gas}} - T_{\text{LN}2}) \frac{y}{2R_o}.$$
 (3.4)

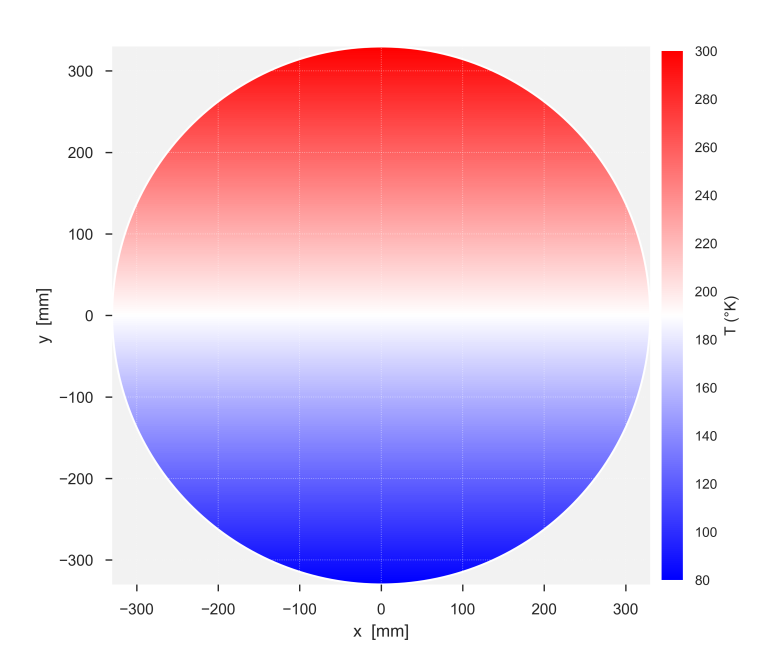


Figure 3.4: Temperature Distribution B: Linear increasing temperature distribution.

Because the vessel is mounted horizontally and the manufacturers filling system delivers the fluid uniformly, temperature variations are expected to depend solely on the vertical coordinate. Moreover, the wall thickness is sufficiently small such that, in agreement with previous experimental evidence (See Sections 2.3 and 2.4), radial gradients can be neglected and the temperature distributions may be treated as uniform across the thickness.

4. Analytical model

During the cooldown process three primary loading effects must be considered: internal pressure, effect of temperature gradient and effect of gravity (or self-weight). Assuming that the tank material is homogeneous, isotropic, and remains within the linear-elastic regime, these load cases can be analyzed independently, and their resulting stress states can be superimposed to obtain the total stress distribution.

Each effect is examined in detail in the following subsections and compared with the results of finite element analyses (FEA). While numerical models allow for greater detail and accuracy, they require access to licensed FEA software, CAD modeling for geometry creation, mesh generation, and computational resources for simulation. This process can be time-consuming and may not always be feasible due to resource constraints. In contrast, analytical methods offer a fast and cost-effective way to obtain an initial picture about the roles of the problem parameters and even quantitative predictions of the representative stress values in the tank. These methods are particularly useful during early design stages or when evaluating multiple design alternatives.

To quantify the individual contributions of each load case, the tank is idealized using simplified mechanical models that capture the dominant behavior. These models are summarized in Figure 4.1. The response to internal pressure is evaluated by modeling the tank as a thin cylindrical shell loaded by internal pressure. The thermal effect on the longitudinal stress is assessed by representing the tank as an Euler-Bernoulli beam subjected to a vertical temperature gradient across the cross-section, setting a low temperature at the bottom and high temperature at the top. The circumferential stress is derived from shell theory only in the cross-section plane. The gravitational effect uses the same beam model as the thermal effect on the longitudinal stress, but this time subjected to a uniformly distributed load.

For simplicity and consistency with literature, stresses due to gravity and thermal gradient are initially computed in a Cartesian coordinate system, while those due to internal pressure are calculated in a cylindrical coordinate system. All significant stress components are then transformed into a common basis and combined in tensorial form. Finally, the von Mises equivalent stress of the combined state is computed to allow for comparison against material strength criteria.

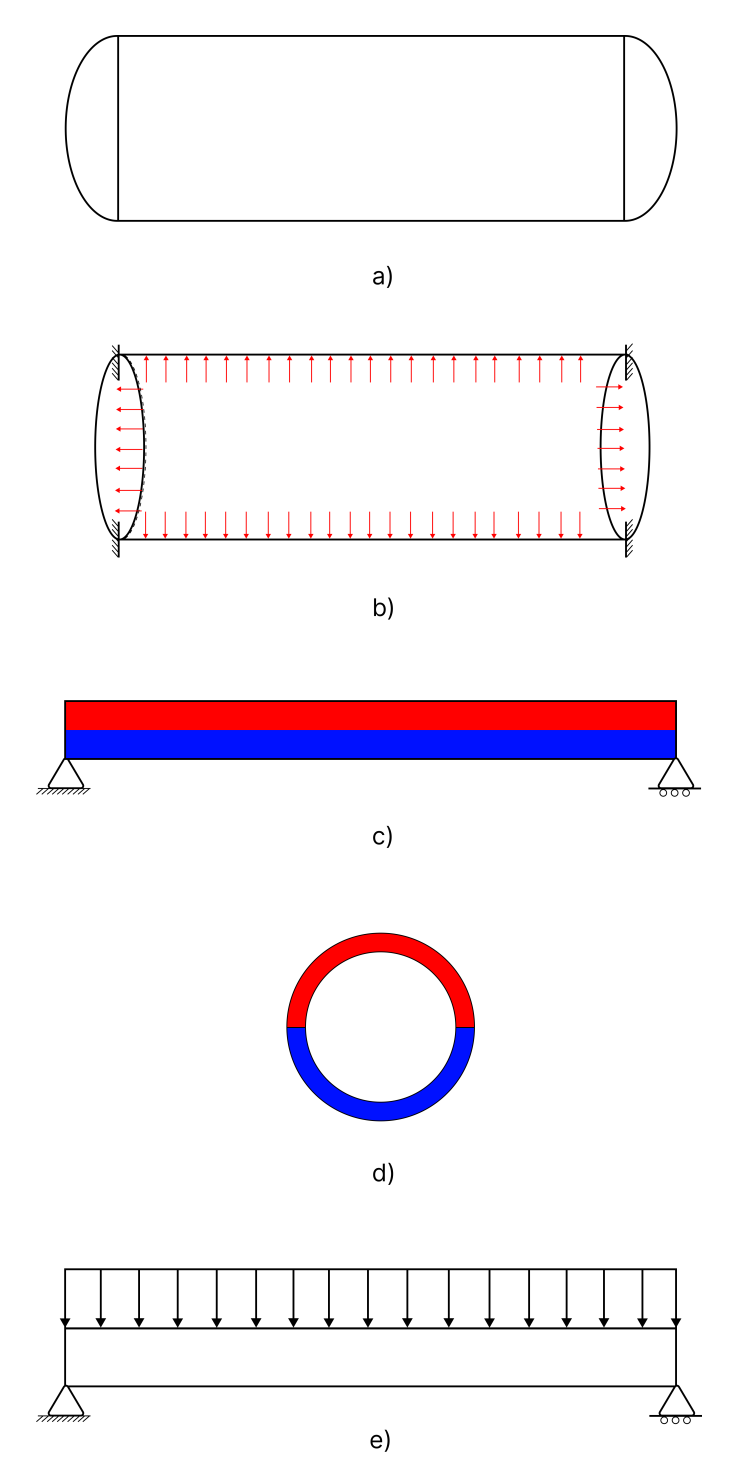


Figure 4.1: Sketches of the analytical models. **a)** Complete tank geometry. **b)** Effect of internal pressure (Model for both longitudinal and circumferential stress). **c)** Effect of temperature (Longitudinal stress). **c)** Effect of gravity.

4.1 Effect of Internal Pressure

We can consider the tank as a cylindrical container of radius R subjected to a distributed force b_r due to internal excess pressure P. A conservative approximation would be to remove the torispherical heads and replace them by rigid end plates. Using the Kirchhoff model, constitutive equations for the shear forces are replaced by Kirchhoff constraints [42]. With the relationship $\theta_{\varphi} = -du_r/dz$ and assuming rotational symmetry, where derivatives with respect φ vanish, and $u_{\varphi} = 0$, the non zero constitutive equations for the stress resultants simplify [42] to

$$N_{zz} = \frac{hE}{1 - \nu^2} \left(\frac{du_z}{dz} - \nu \frac{1}{R} u_r \right) + D \frac{1}{R} \frac{d^2 u_r}{dz^2} , \qquad (4.1)$$

$$N_{\varphi\varphi} = \frac{tE}{1 - \nu^2} \left(\nu \frac{du_z}{dz} - \frac{1}{R} u_r \right), \tag{4.2}$$

$$M_{zz} = -D\left(\frac{d^2u_r}{dz^2} + \frac{1}{R}\frac{du_z}{dz}\right),\tag{4.3}$$

$$M_{\varphi\varphi} = D\left(\nu \frac{d\theta_{\varphi}}{dz} - \frac{u_r}{R^2}\right). \tag{4.4}$$

The relevant equilibrium equations simplify to

$$\frac{dN_{zz}}{dz} = 0,$$

$$\frac{dQ_z}{dz} + \frac{1}{R}N_{\varphi\varphi} + b_r = 0,$$

$$\frac{dM_{zz}}{dz} - Q_z = 0,$$
(4.5)

and after elimination of the shear force (using the moment equation)

$$\frac{dN_{zz}}{dz} = 0 \quad \text{and} \quad \frac{d^2M_{zz}}{dz^2} + \frac{1}{R}N_{\varphi\varphi} + b_r = 0. \tag{4.6}$$

The constitutive equations for $N_{\varphi\varphi}$ and M_{zz} can be expressed in terms of u_r by using the equilibrium and constitutive equations for N_{zz}

$$N_{zz} = \frac{tE}{1 - \nu^2} \left(\frac{du_z}{dz} - \nu \frac{1}{R} u_r \right) + D \frac{1}{R} \frac{d^2 u_r}{dz^2} = N = \text{const} \quad , \tag{4.7}$$

$$\frac{du_z}{dz} = \nu \frac{1}{R} u_r + \frac{1 - \nu^2}{tE} \left(N - D \frac{1}{R} \frac{d^2 u_r}{dz^2} \right). \tag{4.8}$$

Hence after elimination of $\frac{du_z}{dz}$ and with the shorthand notation $a = \frac{h}{R}$

$$N_{\varphi\varphi} = \frac{hE}{1 - \nu^2} \left(\nu \frac{du_z}{dz} - \frac{1}{R} u_r \right) = -\frac{hE}{R} u_r + \nu \left(N - D \frac{1}{R} \frac{d^2 u_r}{dz^2} \right), \tag{4.9}$$

$$M_{zz} = -D\left(\frac{d^2u_r}{dz^2} + \frac{1}{R}\frac{du_z}{dz}\right) = -D\left[\left(1 - \frac{a^2}{12}\right)\frac{d^2u_r}{dz^2} + \frac{1}{R}\frac{1 - \nu^2}{hE}N + \nu\frac{1}{R^2}u_r\right], \quad (4.10)$$

$$\frac{d^2 M_{zz}}{dz^2} + \frac{1}{R} N_{\varphi\varphi} + b_r = -D \left[\left(1 - \frac{a^2}{12} \right) \frac{d^4 u_r}{dz^4} + \nu \frac{2}{R^2} \frac{d^2 u_r}{dz^2} \right] - \frac{hE}{R^2} u_r + \nu \frac{N}{R} + b_r = 0. \quad (4.11)$$

Assuming that the end plates are rigid so that the displacement and rotation vanish at ends of the cylindrical container and $a^2 \ll 1$, the boundary value problem for the transverse displacement (positive inwards) takes the form

$$\frac{d^4 u_r}{dz^4} + \nu \frac{2}{R^2} \frac{d^2 u_r}{dz^2} + \frac{hE}{DR^2} u_r - \frac{1}{D} \left(\nu \frac{N}{R} + b_r \right) = 0 \quad \text{in } (0, L).$$
 (4.12)

The fourth order differential equation can further be simplified by omitting the second derivative term as negligible compared to the fourth order derivative term [42]. Given the cylindrical geometry, N is defined as

$$N = \frac{P\pi R^2}{2\pi R} = \frac{PR}{2}. (4.13)$$

Taking $b_r = -P$, introducing the definition of N, neglecting the second derivative term and reorganizing, the boundary value problem takes the form

$$D\frac{d^4u_r}{dz^4} + \frac{hE}{R^2}u_r = P\left(\frac{\nu}{2} - 1\right) \quad \text{in } (0, L), \tag{4.14}$$

$$u_r = \frac{du_r}{dz} = 0$$
 on $\{0, L\}$. (4.15)

Solving the equation with the respective boundary conditions provides the radial displacement and thereby the forces. Then, uniform membrane stresses are defined by

$$\sigma_{\varphi\varphi_{\text{membrane}}} = \frac{N_{\varphi\varphi}}{h}, \qquad \sigma_{zz_{\text{membrane}}} = \frac{N_{zz}}{h}.$$
 (4.16)

If we introduce a through-thickness coordinate $\zeta \in [-h/2, h/2]$ (positive outwards), normal bending stresses vary linearly with

$$\sigma_{\varphi\varphi}(\zeta) = \sigma_{\varphi\varphi_{\text{membrane}}} - \frac{12 M_{\varphi\varphi}}{h^3} \zeta, \qquad \sigma_{zz}(\zeta) = \sigma_{zz_{\text{membrane}}} - \frac{12 M_{zz}}{h^3} \zeta.$$
 (4.17)

To fulfill the stress state, the shear stress is defined by

$$\tau_{zr} = \frac{Q_z}{h}.\tag{4.18}$$

For this load case, the kinematic quantity of interest is the radial displacement u_r , which will be directly compared against the finite element analysis (FEA) results. This quantity is fundamental, as many other mechanical responses are derived from its accurate prediction. In terms of stress components, the comparison will focus on the axial stress σ_{zz} , the circumferential (hoop) stress $\sigma_{\varphi\varphi}$, and the shear stress τ_{zr} , since together they capture both membrane and bending stress effects.

4.2 Effect of Temperature Gradient

4.2.1 Longitudinal Stress

The global bending response of the vessel is idealised by modelling the tank as an Euler-Bernoulli beam with annular cross-section. That is, every cross-section initially normal to the neutral axis remains plane and normal after deformation [43]. Because the torispherical heads possess a rapidly varying second moment of area that would make the beam model rather complex, each head is replaced by a fictitious cylindrical continuation. The effective beam length therefore becomes

$$L_{\text{beam}} = L + 2(SF + DH),$$

and boundary conditions are imposed at the new ends z = -(SF + DH) and z = L + (SF + DH). The specific support conditions are discussed in Section 6.2. Using Euler-Bernoulli beam theory, as discussed already in Section 2.5.3, the total longitudinal strain varies linearly with the depth coordinate y,

$$\varepsilon_z^{\text{total}}(y) = \varepsilon_0 - \kappa y,$$
 (4.19)

where ε_0 denotes the mid-plane (centroidal axis) strain, and κ is the curvature of the beam's neutral axis. A non-uniform temperature distribution through the beam's thickness induces an additional (thermal) strain given by

$$\varepsilon_z^{\text{th}}(y) = \alpha \, \Delta T(y),$$
 (4.20)

where α is the coefficient of linear thermal expansion, and $\Delta T(y) = T_{\text{ref}} - T(y)$ is the temperature difference from a stress-free reference temperature T_{ref} .

The mechanical (elastic) strain is obtained by subtracting the thermal strain from the total strain:

$$\varepsilon_z^{\text{elastic}}(y) = \varepsilon_0 - \kappa y - \alpha \Delta T(y),$$
(4.21)

which, through Hooke's law, yields the corresponding axial (normal) stress:

$$\sigma_z(y) = E \,\varepsilon_z^{\text{elastic}}(y) = E \left[\varepsilon_0 - \kappa \, y - \alpha \, \Delta T(y)\right],$$
 (4.22)

where E is Young's modulus. It is important to emphasize that the stress distribution is strongly influenced by the temperature profile and, consequently, by the resulting temperature difference $\Delta T(y)$. As discussed in Section 3.3, temperature profile A introduces a discontinuity (jump) at the mid-height of the cross-section. This abrupt change in temperature leads to a corresponding discontinuity in the thermal strain field. Since the beam's mechanical response must satisfy both compatibility (Euler-Bernoulli kinematics) and equilibrium, the mismatch between the imposed thermal strains and the linear strain field assumed by beam theory results in a discontinuity in the axial stress distribution at the same location. In essence, the stress field must accommodate this incompatibility.

The specific values of the axial stress distribution depend on the beam's boundary conditions. For a simply supported-simply supported (SS-SS) beam, there are no constraints preventing longitudinal expansion or rotation. Therefore, the axial force N and bending moment M must vanish over the cross-section Ω due to equilibrium:

$$N = \int_{\Omega} \sigma_z \, \mathrm{d}A = 0, \tag{4.23a}$$

$$M = \int_{\Omega} \sigma_z \, y \, \mathrm{d}A = 0. \tag{4.23b}$$

Substituting Eq. (4.22) into Eq. (4.23a) yields:

$$N = 0 = \varepsilon_0 \int_{\Omega} dA - \kappa_{SS} \int_{\Omega} y \, dA - \alpha \int_{\Omega} \Delta T(y) \, dA,$$

where the subscript $_{SS}$ highlights that the expression pertains to the simply supported configuration. If the y-axis is aligned with the centroid of the cross-section, then

$$\int_{\Omega} y \, \mathrm{d}A = 0, \qquad \int_{\Omega} \mathrm{d}A = A, \tag{4.24}$$

and the mid-plane strain becomes:

$$\varepsilon_0 = \frac{\alpha}{A} \int_{\Omega} \Delta T(y) \, \mathrm{d}A. \tag{4.25}$$

Similarly, substituting Eq. (4.22) into Eq. (4.23b) gives:

$$M = 0 = \varepsilon_0 \int_{\Omega} y \, dA - \kappa_{SS} \int_{\Omega} y^2 \, dA - \alpha \int_{\Omega} \Delta T(y) \, y \, dA.$$

Using Eq. (4.24) and defining the second moment of area as $I = \int_{\Omega} y^2 dA$, the curvature of the simply supported beam is found to be

$$\kappa_{SS} = -\frac{\alpha}{I} \int_{\Omega} \Delta T(y) y \, dA = \kappa_0, \tag{4.26}$$

where we will denote κ_0 the curvature that the beam would adopt in a free (unconstrained) thermal deformation.

In contrast, consider a clamped-simply supported (C-SS) beam. In this case, the beam is restrained against rotation and vertical displacement at one end, and only vertical displacement at the other. The configuration introduces an internal moment reaction at the clamped end, making the problem statically indeterminate (three unknown reactions and only two equilibrium equations). To solve this, we can conceptually replace the simply supported end with a vertical reaction force R. The bending moment along the beam is then expressed as

$$M(z) = R(L - z) = EI\kappa(z) = EI(w''(z) - \kappa_0),$$
 (4.27)

where w(z) is the transverse displacement of the neutral axis and w''(z) its second derivative. Solving for the second derivative

$$w''(z) = -\left(\frac{R}{EI}\right)z + \left(\frac{RL + EI\kappa_0}{EI}\right). \tag{4.28}$$

Integrating twice and applying the clamped boundary conditions w(0) = w'(0) = 0, we obtain the displacement w(z). Enforcing the condition w(L) = 0, which reflects the vertical constraint at the simply supported end, allows us to determine the reaction force R, and hence w''(z) and $\kappa(z)$.

Once the curvature $\kappa(z)$ is known, the axial stress distribution for the C-SS beam follows from Eq. (4.21). Notably, the mid-plane strain ε_0 remains the same as in the SS-SS case, since neither configuration imposes longitudinal displacement constraints. This completes the derivation of the axial stress under combined thermal loading and structural boundary conditions.

For this model, the kinematic quantity of interest is the vertical displacement u_y , which will be directly compared against the finite element analysis (FEA) results. This quantity is fundamental, as the beam model depends on its correct prediction. In terms of stress components, the comparison will focus on the axial stress σ_{zz} .

4.2.2 Circumferential Stress

We have defined the temperature to be non-axisymmetrical and depend solely in the circumferential coordinate. To estimate the stresses, the framework developed by Logie and Coventry [36] is reproduced here. This framework assumes a cylindrical body far away from boundary constraints with the temperature having the following equation

$$T_{\varphi} = \sum_{n=1}^{\infty} \left(A_n r^n + B_n r^{-n} \right) \cos n\varphi + \left(C_n r^n + D_n r^{-n} \right) \sin n\varphi. \tag{4.29}$$

Given the harmonic steady-state condition, the effort required in minimising the sum (integral) of the squares of the differences over the entire cross sectional area of the tube can be reduced by seeking Fourier series of Equation (4.29) only at $r = R_i$ and $r = R_o[36]$

$$T_{i} = \overline{T}_{i} + \sum_{n=1}^{\infty} B'_{n} \cos n\varphi + D'_{n} \sin n\varphi ,$$

$$T_{o} = \overline{T}_{o} + \sum_{n=1}^{\infty} B''_{n} \cos n\varphi + D''_{n} \sin n\varphi .$$

$$(4.30)$$

Boley and Weiner [30] proved that only terms of a plane harmonic temperature distribution for which n = 0 and n = 1 contribute to the stress components. To obtain the parameters, the temperature distributions from Section 3.3 are expanded using fourier series representation, and then the components corresponding to n = 0 and n = 1 are

applied. With this result, the circumferential stress resulting from the condition of non-axisymmetrical heating is given by

$$\sigma_{\varphi\varphi} = K \frac{\alpha E}{2(1-\nu)} \left[1 - \ln \frac{R_o}{r} - \frac{R_i^2}{R_o^2 - R_i^2} \left(1 + \frac{R_o^2}{r^2} \right) \ln \frac{R_o}{R_i} \right] + K_{\varphi} \frac{\alpha E}{2(1-\nu)} \left(3 - \frac{R_i^2 + R_o^2}{r^2} - \frac{R_i^2 R_o^2}{r^4} \right),$$
(4.31)

where K is used to describe the various axisymmetrical and nonaxisymmetrical geometrical temperature contributions. The contribution of n=0 to stress from the average surface temperature difference is

$$K = \frac{\overline{T}_i - \overline{T}_o}{\ln \frac{R_o}{R_i}} \,, \tag{4.32}$$

and the contribution of n = 1 comes from

$$K_{\varphi} = \frac{rR_{i}R_{o}}{R_{o}^{2} - R_{i}^{2}} \left[\left(\frac{B_{1}'R_{o} - B_{1}''R_{i}}{R_{i}^{2} + R_{o}^{2}} \right) \cos \varphi + \left(\frac{D_{1}'R_{o} - D_{1}''R_{i}}{R_{i}^{2} + R_{o}^{2}} \right) \sin \varphi \right]. \tag{4.33}$$

Since this model is already formulated in the plane, there are no relevant kinematic quantities to analyze. Therefore, the comparison with the numerical (FEA) model focuses exclusively on the circumferential stress component $\sigma_{\varphi\varphi}$.

4.3 Effect of Gravity

To assess the stresses generated by self-weight and by the weight of the cryogen (liquid nitrogen during initial cooldown), the same beam idealisation introduced for the thermal case is retained. The beam is now subjected to a uniform distributed load p, as sketched in Figure 4.1e. This load combines the weight of the fluid and the weight of the metallic shell

$$p = \rho_{\text{fluid}} g A_{\text{fluid}} + \rho_{\text{steel}} g A_{\text{solid}}, \tag{4.34}$$

where g is the acceleration of gravity, ρ_{fluid} and A_{fluid} are the fluid density and the internal cross-sectional area, and ρ_{steel} and A_{solid} are the steel density and the shells solid cross-sectional area.

For this model, the cartesian coordinate system will be used. The centroidal axis of the beam coincides with the z-axis, y is taken positive upward in the cross-sectional plane and x points in-plane. If we use the Euler-Bernoulli kinematic assumption that plane cross-sections remain plane and normal to the deformed beam axis, the curvature in the z-y plane is proportional to the bending moment about the x-axis [40]

$$\frac{d^2v}{dz^2} = \frac{M_x(z)}{E I_x},\tag{4.35}$$

where v(z) is the transverse deflection and

$$I_x = \iint\limits_{\Omega} y^2 \, dA \,\,, \tag{4.36}$$

is the second moment of area of the cross-section Ω about the neutral x-axis. Because the distributed load p(z) is assumed to remain constant over an infinitesimal segment dz (a standard assumption in first-order beam theory), vertical force and moment equilibrium give

$$\frac{dV_y(z)}{dz} = -p(z), \qquad \frac{dM_x(z)}{dz} = -V_y(z), \tag{4.37}$$

with $V_y(z)$ the internal shear force (positive upward) and M(z) the bending moment about the x-axis. Eliminating $V_y(z)$ from (4.37) yields the load-moment relation

$$\frac{d^2 M_x(z)}{dz^2} = p(z). {(4.38)}$$

Substituting (4.38) into the curvature expression (4.35) produces the Euler-Bernoulli beam equation for transverse deflection:

$$\frac{d^2}{dz^2} \left(E I_x \frac{d^2 v}{dz^2} \right) = p(z). \tag{4.39}$$

Integrating (4.39) four times and applying the appropriate boundary conditions provides v(z), the slope $\theta(z) = dv/dz$, the bending moment M(z) and the shear force V(z).

The normal (bending) stress distribution across any section

$$\sigma_z(y) = -\frac{M_x(z) \ y}{I_x},\tag{4.40}$$

follows directly from elementary flexure theory, showing a linear variation with the distance y from the neutral axis. Finally, the shear stress is defined by

$$\tau_{zy}(y) = \frac{V_y(z)}{A}. (4.41)$$

where A is the cross-sectional area of the beam. The constant shear stress expression above is often replaced by a more refined formulation derived from two-dimensional elasticity theory. For a detailed derivation, the reader is referred to standard texts in mechanics of materials, such as Hibbeler's textbook [44]. Under the same transverse shear force V_y , the shear stress distribution across the height y of the cross-section follows a parabolic profile. It vanishes at the outer surfaces (i.e., at $y = \pm R$) and reaches a maximum at the neutral axis.

Similar to the thermal longitudinal stress case discussed previously, the kinematic quantity of interest in this model is the vertical displacement u_y , which will be directly compared against the finite element analysis (FEA) results to validate the beam theory assumptions. This displacement is fundamental, as the accuracy of the beam model relies on its correct prediction. Regarding stress components, the comparison focuses on the axial stress σ_{zz} .

5. Finite-Element Analysis (FEA)

All FE simulations were performed in the commercial finite element software *LS-DYNA*. The dimensional data correspond to the geometry described in Section 3.1 and the material properties are provided in Section 3.2. Model-specific parameters are presented in the following subsections, organized according to the model to which they apply.

5.1 Solver

The filling process is relatively slow compared to the characteristic timescales of the processes governing thermomechanical equilibrium. As a result, the system can be reasonably approximated as quasi-static or steady-state, allowing all time derivatives to be neglected. This simplification leads to a system of linear equations, which can be efficiently solved using direct matrix methods.

5.2 Element formulation

When analyzing thin-walled structures such as cylinders in finite element analysis (FEA), the use of shell elements is strongly justified over solid elements due to both computational efficiency and the ability to accurately capture the structural behavior [45]. Shell elements are specifically formulated to model thin structures, where the thickness is much smaller than the other dimensions, and are mathematically two-dimensional but spatially three-dimensional, making them ideal for representing thin cylinders [46].

Solid elements, while theoretically more precise, require a very fine mesh with multiple elements through the thickness to accurately capture bending behavior. This dramatically increases the computational resources required, often making the analysis impractical for larger models or complex load cases [45]. In contrast, shell elements can simulate the bending and membrane behavior of thin-walled bodies with far fewer elements, resulting in significant savings in computational time and memory, while still providing reliable stress and displacement results for thin structures.

For this reason, geometries were meshed with fully-integrated shell elements (ELFORM = 16). This formulation offers superior accuracy, hourglass control and numerical robustness compared with the default Belytschko-Tsay element (ELFORM = 2) at the expense of additional computational cost [47]. The shell thickness was set to h = 5 mm.

5.3 Mesh

The mesh was constructed with quadrilateral elements with an in-plane edge length of 5 mm. A symmetry plane was used to reduce the mesh size, as shown in Figure 5.1. The mesh was created in the software $Altair\ Hypermesh$ and exported to the solver LS-DYNA.

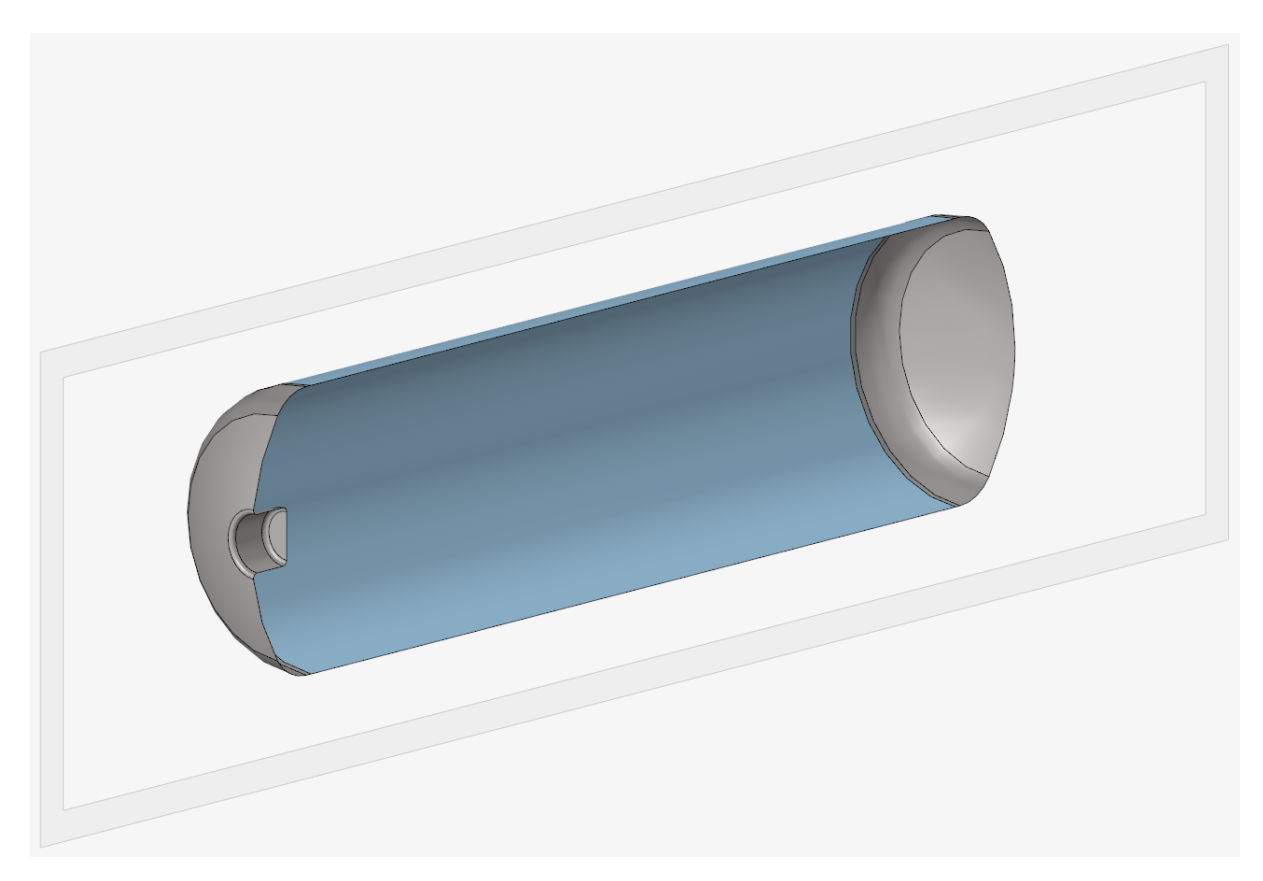
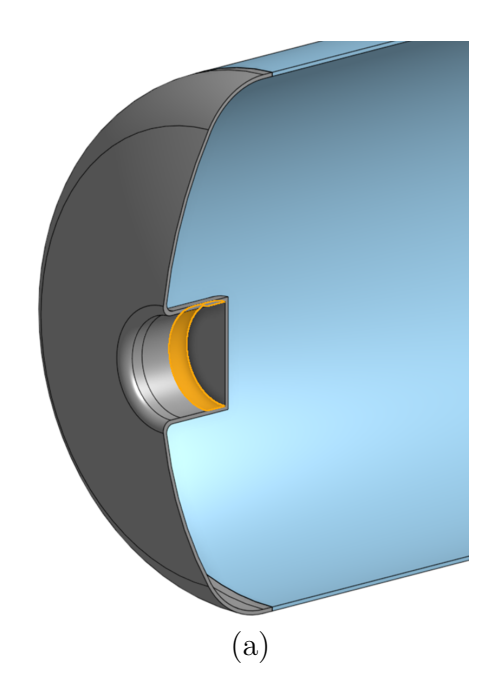


Figure 5.1: Selected symmetry plane in order to reduce mesh size.

5.4 Boundary conditions

The boundary conditions applied to the geometry are depicted in Figure 5.2a. The left torispherical cap is welded to a bearing within the highlighted region. This interface is modeled as a fully fixed boundary condition, constraining all translational and rotational degrees of freedom. On the right end, a single node located at the center of the torispherical cap (see Figure 5.2b) is constrained only in the vertical direction, while all other degrees of freedom remain unrestrained.

Due to confidentiality constraints, the exact configuration of the right cap fixation mechanism cannot be disclosed. In practice, the support is not entirely rigid but permits minimal vertical displacement. Nevertheless, the idealized fixed condition employed in the model is more restrictive and, therefore, conservative. Since the analysis primarily focuses on the behavior of the cylindrical section of the vessel, this simplification does not compromise the validity or relevance of the results.



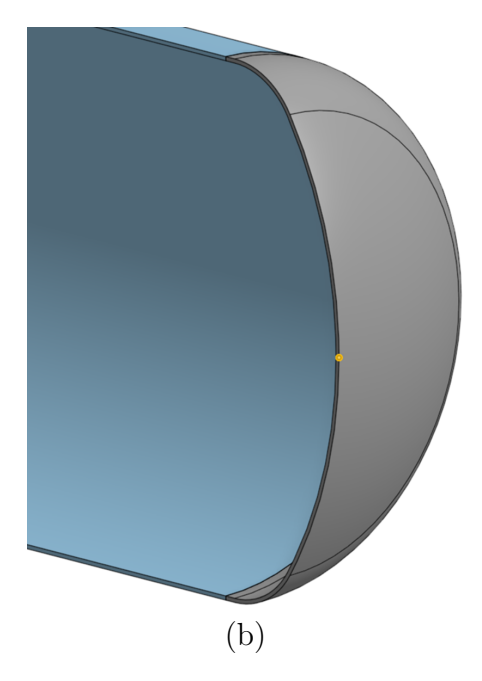


Figure 5.2: Boundary conditions applied to the complete geometry. **a)** The left torispherical cap is fixed at the interface with the bearing (highlighted region). **b)** The right cap is vertically constrained at the center node (highlighted node).

The nodes located on the symmetry plane have constrained translation in the direction normal to the plane —namely, the x-axis. Additionally, their rotations about the y- and z-axes are restricted. All other translational and rotational degrees of freedom remain unconstrained.

5.5 Loading scenarios

Each of the three effects was applied independently, analyzed individually, and then combined into a coupled-effect simulation.

5.5.1 Pressure

A uniform internal pressure of $P_{\text{max}} = 2$ MPa was applied. In the software, the *LOAD_SHELL_SET card was used, with the shell set encompassing all elements of the tank. The pressure acts along the outer normal direction of each element.

5.5.2 Thermal

Temperature distribution is imposed with card *LOAD_THERMAL_VARIABLE_NODE by using the nodal y coordinates to assign a temperature to each node according to the selected thermal profile. The temperature is assumed independent of the x and z directions, accounting for a uniform cooling distribution along the longitudinal axis. A Python script processes the output mesh file, identifies the y coordinate of each node, and assigns the corresponding temperature. The temperature distributions are described in detail in Section 3.3.

5.5.3 Gravity

In the software, the *LOAD_BODY_Y card was used. To represent the liquid filled up to a certain height, the concept of "artificial density" $\rho_{\text{artificial}}$ was introduced:

$$\rho_{\text{artificial}} = \frac{\rho_{\text{fluid}} A_{\text{fluid}} + \rho_{\text{solid}} A_{\text{solid}}}{A_{\text{solid}}}.$$
 (5.1)

The artificial density is evenly distributed, assuming the tank was filled to its mid-height. It is important to note that when a tank is partially filled with water, the internal walls and base are subjected to hydrostatic pressure, a pressure that increases linearly with depth due to the weight of the liquid above each point. In FEA this hydrostatic loading is typically modeled as a pressure distribution applied to the inner surfaces of the tank. This approach accurately represents the true physical loading, as the gauge pressure is zero at the water surface and reaches a maximum at the bottom, resulting in a triangular or trapezoidal pressure profile on the tank walls.

Using an artificial density, where the density of the tank material is increased to account for the water's weight approximates the total vertical load but does not replicate the actual distribution or direction of hydrostatic pressure. While this method simplifies the model by converting the effect of the water into an equivalent self-weight, it neglects the lateral pressure exerted by the liquid on the tank walls and the varying nature of the load with depth. However, in FEA, this approximation can be appropriate when the interest is in the global bending response due to the combined weight of the tank and water (as is the current case), rather than the detailed local stresses from hydrostatic pressure. The artificial density approach reduces modeling complexity and computational effort, making it a practical choice for when computational resources are limited and even more, if the effect of the gravity is expected to be low in comparison with other loadings present in the system.

6. Results: Comparison of Analytical and Numerical Models

A Python script was developed to implement and evaluate the analytical model equations. As shown in Figure 6.1, the script defines a grid of points along both the longitudinal and circumferential directions, where the analytical expressions are computed. In the numerical FEA model, shell elements provide contour plots for the inner, middle, and outer surfaces of the shell. For consistency, the outer layer values were selected for comparison. A summary of the load cases, model types, load application methods, and the quantities compared between the analytical and numerical models is provided in Table 6.1.

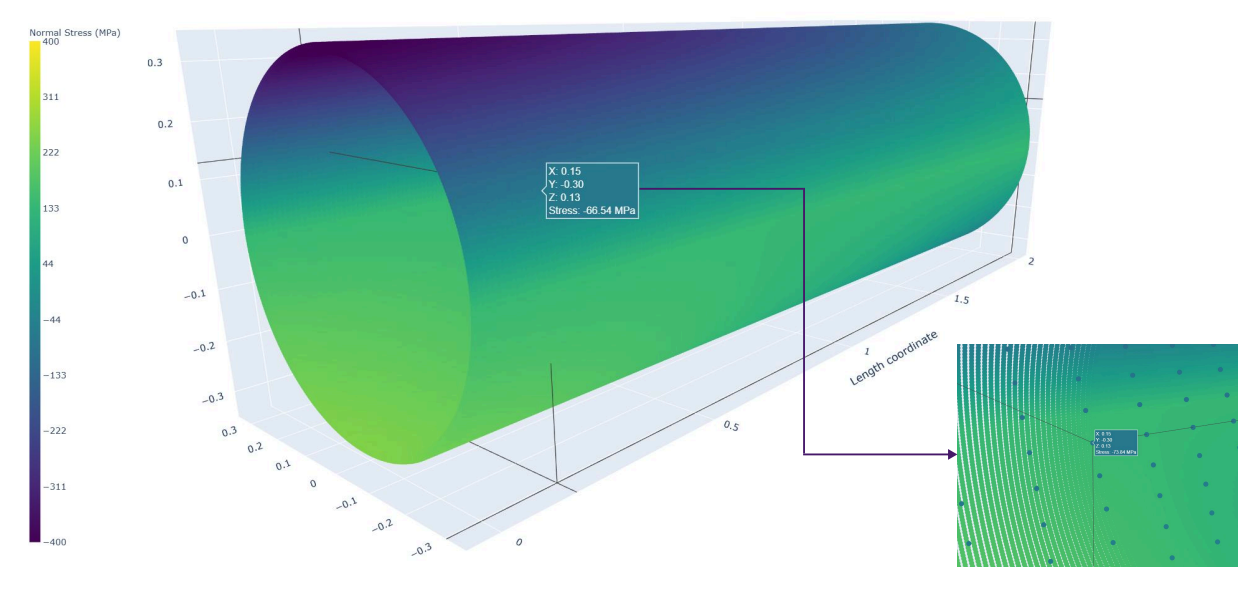


Figure 6.1: Python interactive 3D plot of stress at nodes.

Table 6.1: Summary of analytical models and quantities for comparison with FEA results.

Load Case	Model	Load Application	Kinematics	Stress Components
Pressure	Shell Model	Thin cylindrical tank with closed caps subjected to internal pressure	u_r	$\sigma_{zz},\sigma_{\varphi\varphi},\sigma_{zr}$
Thermal (Longitudinal)	Beam Model	Euler–Bernoulli beam subjected to temperature gradient in the vertical direction	u_y	σ_{zz}
Thermal (Circumferential)	Planar Thermoelasticity	Cross-section of thin cylinder, far from boundaries, subjected to temperature gradient in the vertical direction	_	$\sigma_{arphiarphi}$
Gravity	Beam Model	Euler–Bernoulli beam subjected to uniformly distributed load	u_y	σ_{zz}

The base geometry described in Section 3.1 was derived from a demonstrator developed within a European project and is representative of dimensions commonly used in industry. In this study, two key parameters were varied to assess their influence on the structural response. The first parameter was the length-to-diameter ratio, initially set to $L/D \approx 3$. To investigate the influence of increased slenderness on the applicability of beam models, an additional configuration with a length of 10 m and the same diameter of 0.66 m was analyzed, resulting in $L/D \approx 15$.

The second parameter, related to material properties rather than geometry, was the stiffness of the torispherical end caps. Two cases were considered: one with fully elastic behavior using a Young's modulus of 200 GPa, and another assuming perfectly rigid caps. This variation aimed to examine how substituting the end caps with boundary conditions affects the results. The use of rigid caps in the finite element analysis (FEA) enabled a clearer assessment of this assumption.

While the present study focused on the aforementioned parameters, further variations—particularly in geometry— could provide additional insights into the limitations of the analytical models. For instance, the wall thickness was held constant throughout the analysis. Exploring a range of thicknesses would help identify the validity limits of the thin-shell assumption and determine the extent to which the shell model, which inherently neglects radial stress, remains applicable. Moreover, investigating tanks with shorter lengths could further elucidate the boundaries of the beam theory's applicability. Different geometrical configurations are likely to yield varying degrees of agreement with the analytical solutions.

6.1 Pressure

Figure 6.2 compares the radial displacement caused by internal pressure as obtained from the analytical model and from two finite-element variants. The analytical curve starts from zero at the weld seam, confirming that the clamped boundary condition has been imposed correctly, whereas the numerical model with elastic torispherical heads begins at about 0.088 mm because the cap flexibility allows a slight displacement on the weld seam. The analytical solution reaches its maximum of 0.19 mm at 100 mm from the weld, while the numerical prediction peaks at 0.196 mm and is shifted to 60 mm from the weld seam.

Farther along the cylinder, both curves converge toward a nearly constant displacement of 0.18 mm analytically and 0.19 mm numerically. This convergence illustrates the attenuation of the edge-induced bending described in Section 4.1. To isolate the influence of cap compliance, a second numerical simulation was performed using perfectly rigid heads. As anticipated, the displacement at the weld drops to zero, and the peak as well as the stabilized region closely match the analytical prediction. This confirms that the kinematic discrepancy between the analytical and numerical models originates primarily from the compliance of the caps.

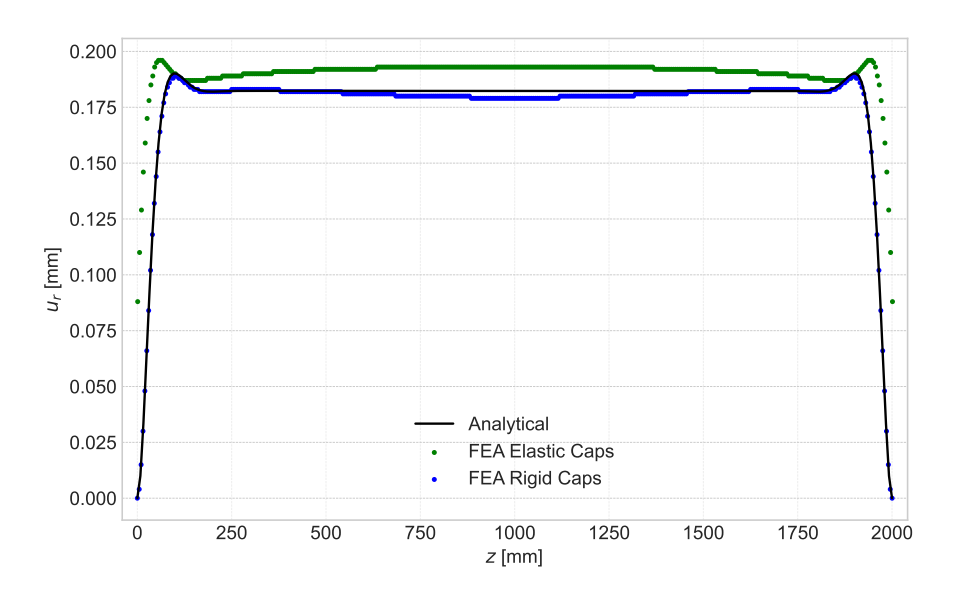


Figure 6.2: Radial displacement u_r due to internal pressure: analytical solution and finite-element models with compliant and rigid torispherical heads.

Since the pressure load case is axisymmetric, the stress results are presented as 2D plots rather than 3D contour plots, as this representation facilitates a more precise quantitative comparison of stress levels between the analytical and numerical models.

6.1.1 Longitudinal Stress

The longitudinal stress distribution in the outer layer predicted by the analytical and numerical models is plotted along the axial coordinate in Figure 6.3. Part (a) shows the global response of the cylindrical shell: both curves converge to 65.5 MPa, in excellent agreement with the classical thin-walled-vessel expression $\sigma_{zz} = PR_m/(2h)$ for regions sufficiently far from the head-shell junction [44]. The profile is nearly symmetric about the mid-span.

Part (b) enlarges the vicinity of the weld seam. When the finite-element model retains the actual stifness of the torispherical heads, it predicts an initial tensile stress of $100\,\mathrm{MPa}$, which decays to $65.5\,\mathrm{MPa}$ within $0.15\,\mathrm{m}$. The analytical solution, however, begins at a compressive value of $-136\,\mathrm{MPa}$, rises to a tensile peak of $107\,\mathrm{MPa}$ at $0.05\,\mathrm{m}$, and then approaches the same nominal stress. This discrepancy is attributed to the compliance of the heads. When the heads are idealized as rigid in the numerical model, the trend approaches the analytical prediction, yet the numerical solution still underestimates the compressive stress at the weld: the rigid-cap model yields $-32.5\,\mathrm{MPa}$ at the junction, climbs to $90\,\mathrm{MPa}$ at $0.05\,\mathrm{m}$, and stabilizes at $65.5\,\mathrm{MPa}$ by $0.15\,\mathrm{m}$.

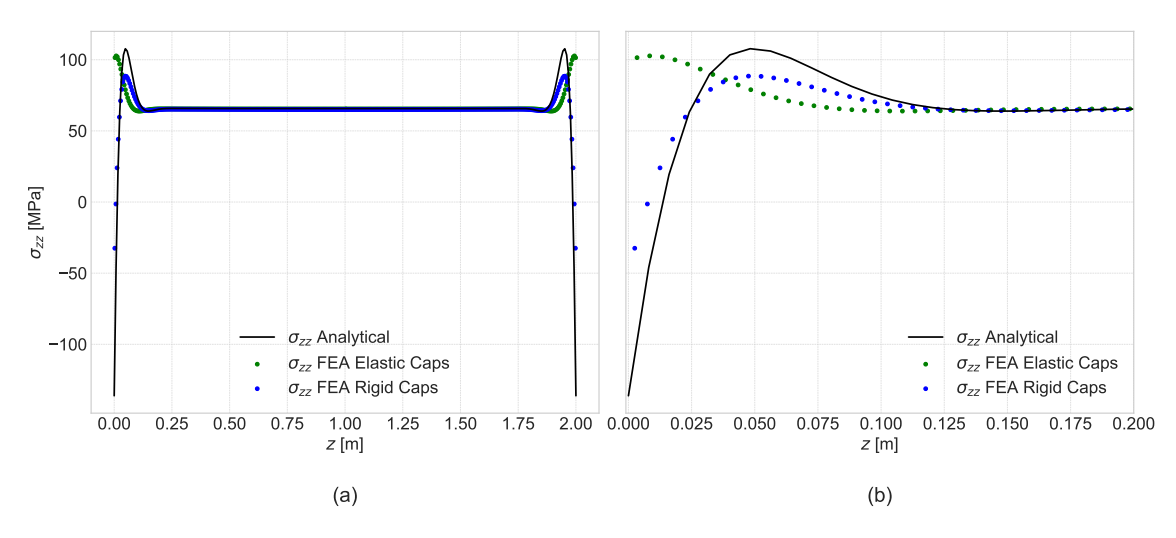


Figure 6.3: Longitudinal stress σ_{zz} along the cylinder under internal pressure. (a) Global distribution showing both analytical and finite-element results. (b) Enlarged view of the boundary.

The stresses presented thus far correspond to the external layer of the shell wall. According to Eq. (4.17), the stresses due to internal pressure are defined by the superposition of a constant membrane component and a linearly varying bending component. Because the bending component changes sign across the thickness, the resulting stress near the boundary changes. At the outer surface, membrane and bending stresses add, producing the maximum compressive value. At the mid-surface the bending term vanishes, so the stress reduces to the membrane value, which is the uniform stress observed far from the head-shell junction. At the inner surface the bending term reverses sign, turning the boundary stress from compression to tension. As the membrane component is thickness-independent and the steepest stress gradients occur at the outer surface, the remainder of the analysis focuses on that layer of the vessel wall.

6.1.2 Circumferential Stress

The circumferential stress distribution in the outer layer, obtained from both the analytical formulation and the finite-element model, is plotted against the axial coordinate in Figure 6.4. Figure 6.4(a) shows the global response of the cylindrical shell: the two predictions converge to 131 MPa, matching the classical thin-walled-vessel formula $\sigma_{\varphi\varphi} = PR_m/h$ for regions sufficiently far from the head-shell junction [44]. The trend mirrors that of the longitudinal stress, with pronounced peaks near the heads, a uniform plateau in the mid-span, and symmetry about the shells mid-length.

Figure 6.4(b) enlarges the stress field in the vicinity of the weld seam. When the finite-element model preserves the actual flexibility of the torispherical heads, the circumferential stress starts at 89 MPa (tension), rises to a peak of 140 MPa within $0.05 \,\mathrm{m}$, and then decays to the membrane value of 131 MPa at about $0.15 \,\mathrm{m}$. The analytical solution begins at a much lower tensile level of 20 MPa, reaches its maximum of 135 MPa around $0.09 \,\mathrm{m}$, and ultimately converges to the same nominal stress. This discrepancy is attributed to the compliance of the heads. Idealising the heads as rigid in the numerical model brings the prediction closer to the analytical trend, although it now underestimates the tensile stress at the seam, even producing a slight compressive value of $-8.4 \,\mathrm{MPa}$. From this point the stress climbs rapidly to $136 \,\mathrm{MPa}$ at $0.09 \,\mathrm{m}$ and stabilises at $131 \,\mathrm{MPa}$ by $0.15 \,\mathrm{m}$.

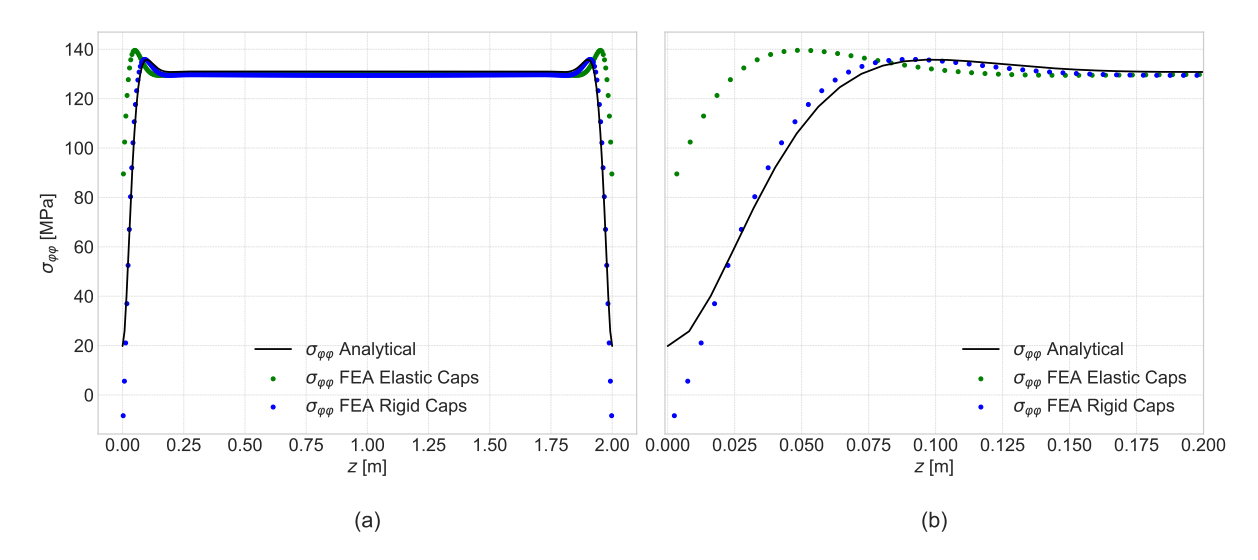


Figure 6.4: Circumferential stress $\sigma_{\varphi\varphi}$ along the cylinder under internal pressure. (a) Global distribution showing both analytical and finite-element results. (b) Enlarged view of the boundary.

The only substantive discrepancies between the elastic-cap simulation and the analytical solution are therefore traced to the extra flexibility of the real torispherical heads, which alleviates the boundary-induced zone while leaving the global membrane response unchanged.

6.1.3 Stress Tensor

In practical applications, the radial (through-thickness) stress component corresponds to the normal stress induced by the internal pressure. However, within the shell theory framework, this radial stress is considered to be zero. In contrast, the in-plane shear stress, expressed by Eq. (4.18), does not necessarily vanishes, and it is presented in Figure 6.5.

When the torispherical heads are represented with their actual stiffness, the finite-element model predicts a peak shear of $1.2\,\mathrm{MPa}$ at the weld seam; the magnitude drops to zero at the cylinder mid-span, and the distribution is antisymmetric about that midplane. By contrast, both the closed-form (analytical) solution and the finite-element model with idealised rigid heads give the same profile, peaking at $10\,\mathrm{MPa}$ in the left head and $-10\,\mathrm{MPa}$ in the right head before vanishing once the edge effect has decayed. The difference between the two numerical solutions therefore stems from the additional compliance introduced by the real heads, an effect neglected in the analytical formulation.

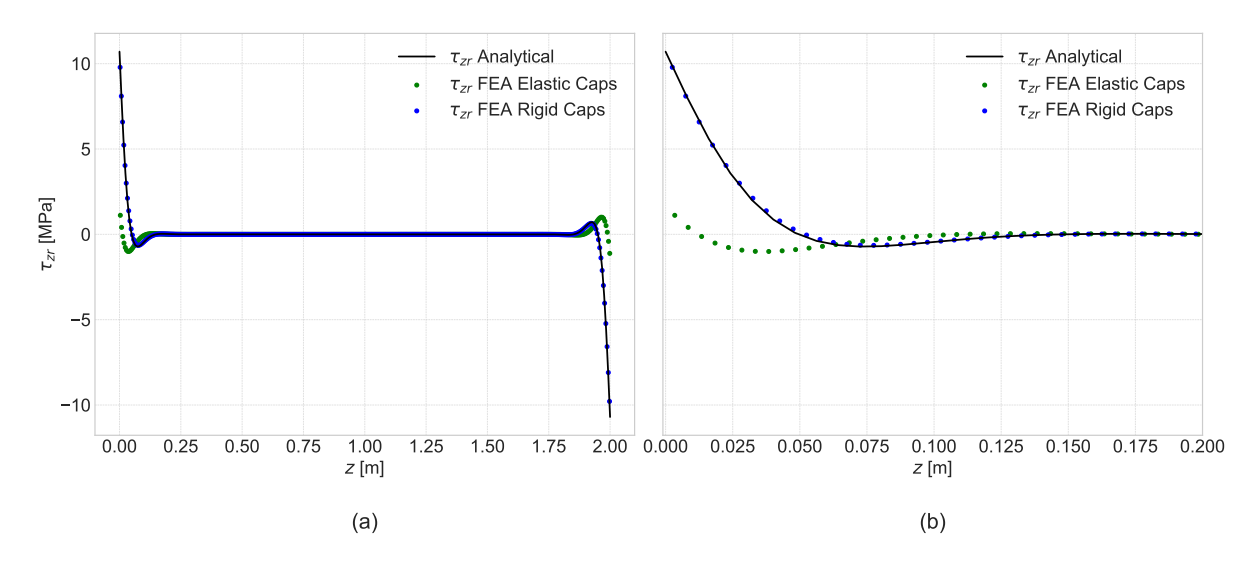


Figure 6.5: Shear stress τ_{zr} along the cylinder under internal pressure. (a) Global distribution showing both analytical and finite-element results. (b) Enlarged view of the boundary.

While the analytical model reproduces the stresses accurately in regions remote from the boundaries, it over-predicts the local peaks obtained with elastic caps: it yields compressive longitudinal stresses where the compliant-head model shows tension, underestimates the tensile hoop stress at the weld, and overstates the shear by nearly an order of magnitude. Because these shear stresses are two orders of magnitude smaller than the corresponding circumferential and longitudinal components, the components of the analytical stress tensor may be simplified to

$$\boldsymbol{\sigma}_{\text{pressure}}^{\text{analytical}} = \begin{bmatrix} \sigma_{\varphi\varphi} & \tau_{\varphi r} & \tau_{\varphi z} \\ \tau_{r\varphi} & \sigma_{rr} & \tau_{rz} \\ \tau_{z\varphi} & \tau_{zr} & \sigma_{zz} \end{bmatrix} = \begin{bmatrix} \sigma_{\varphi\varphi} & 0 & 0 \\ 0 & \sigma_{rr} & \tau_{rz} \\ 0 & \tau_{zr} & \sigma_{zz} \end{bmatrix} \approx \begin{bmatrix} \sigma_{\varphi\varphi} & 0 & 0 \\ 0 & 0 & 0 \\ 0 & 0 & \sigma_{zz} \end{bmatrix}.$$
(6.1)

6.2 Thermal

6.2.1 Longitudinal Stress

Figure 6.6 shows the vertical displacement field u_y that develops under the temperature gradient A. Finite-element results obtained with elastic torispherical heads (Figure 6.6a) reveal a marked variation over the cross-section: the mid-height line deflects by about 3.2 mm, the bottom fibre by 1.6 mm, and the top fibre by only 0.75 mm. The cross-sectional average peaks near 3.0 mm. Because such behaviour is driven by local shell distortion rather than by bending of the centroidal axis, it cannot be reproduced by a classical Euler-Bernoulli beam model. The cross-section deformation is recognized with the deformed shape of the tank.

Although the left end of the numerical model is formally clamped, the overall deflected shape is close to parabolic, as if the cylinder were simply supported at both ends. Guided by this observation, a simply-supported/simply-supported (SS-SS) analytical beam model was introduced. It predicts both the magnitude and the longitudinal position of the average cross-section displacements far better than the original clamped/simply-supported (C-SS) model, yet it still fails to capture the large spread between the top and bottom fibres because it neglects cross-section warping.

To isolate the influence of end-cap flexibility, a second simulation was performed with perfectly rigid torispherical heads. In this case the displacement at the left end drops to zero, the global curvature is in better agreement with the C-SS analytical solution, and the overall amplitudes decrease. The cross-sectional spread is reduced but still present, so the response approaches that of a classical beam in which deformation follows the centreline. This is supported as well by the deformed shape of the tank. The comparison confirms that the compliance of the torispherical heads effectively transforms the nominal clamp into a simple support and amplifies the role of shell distortion.

Having established that the vessel global behavior can be approximated as a simply supported beam, the longitudinal-stress comparison can be restricted to the FEA results and the simply-supported/simply-supported (SS-SS) analytical solution.

Figure 6.7 presents the axial stress distribution σ_{zz} along the cylindrical section of the 2 m tank equipped with elastic heads. The results exhibit a distinct stress peak near the temperature transition region. As discussed in Section 4.2.1, this behavior is characteristic of Temperature Profile A. The step-wise change in temperature difference (ΔT) at mid-height—specifically, $\Delta T=0$ above the interface and $\Delta T=-220$ K below—induces a discontinuity in the elastic strain (see Eq. (4.21)), and consequently in the stress distribution. This discontinuity arises from the mismatch between the thermally induced strain and the total strain governed by beam kinematics.

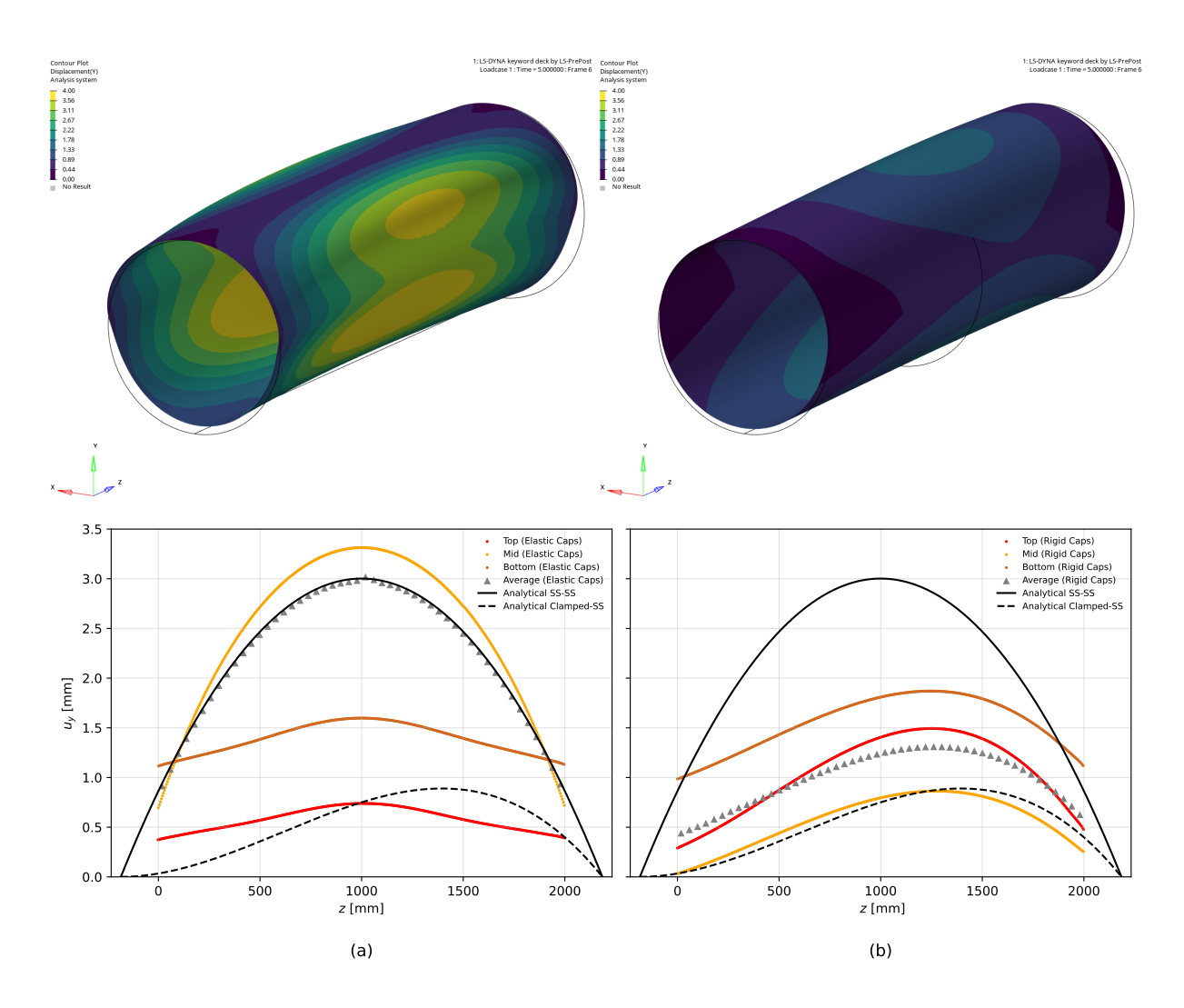


Figure 6.6: Vertical displacement u_y under thermal loading: finite-element results with **a)** normally stiff and **b)** rigid heads compared with clamped-simply-supported (C-SS) and simply-supported-simply-supported (SS-SS) analytical beam models. The undeformed outline is shown in black; deformations are magnified 20 for clarity.

Focusing at the midspan $z=1000\,\mathrm{mm}$, the results of the FEA model give a tension of 25 MPa at the crown, compression of $-213\,\mathrm{MPa}$ just above the temperature interface, tension of 216 MPa just below the interface in the cold zone, and mild compression of $-30\,\mathrm{MPa}$ at the keel. This sequence of tension, compression, tension, compression from top to bottom of the cross section persists almost unchanged over the full length, only attenuating slightly near the boundaries. The stress pattern, better appreciated in Figure 6.8, becomes clear by inspecting Eq. (4.22). The mid-plane strain ε_0 is negative (reflecting overall contraction during cooldown), and uniform across the section because there is no net axial force. The curvature κ is negative (the shell arches upward) and constant because the SS-SS supports carry zero bending moment.

First, in the crown, y is largest and positive. The term $-\kappa y$ is therefore strongly positive and outweighs the negative ε_0 , giving a net tensile elastic strain despite the contraction of the mid-plane. Physically, this means that the tension on the top fibers due to the concave downward shape outweighs the contraction of the midplane due to the overall cooling down.

Following with the warm mid-height region (just above the interface), where $y \approx 0$, the stress is governed almost entirely by ε_0 , hence strongly compressive. Next, at the cold mid-height (just below the interface), the local temperature drop ΔT is large and negative. If this zone were free to deform, it would contract more than the mid-plane, so the internal constraint (continuity between the material) produces a tensile stress.

Finally, at the keel, the component $\varepsilon_0 - \kappa y$ is now most negative, which means that the fibers in the lower bottom are mostly in compression due to the deformed final shape of the tank. Part of the compression is explained by the thermal contraction, so this gives a low (but still compressive) elastic stress.

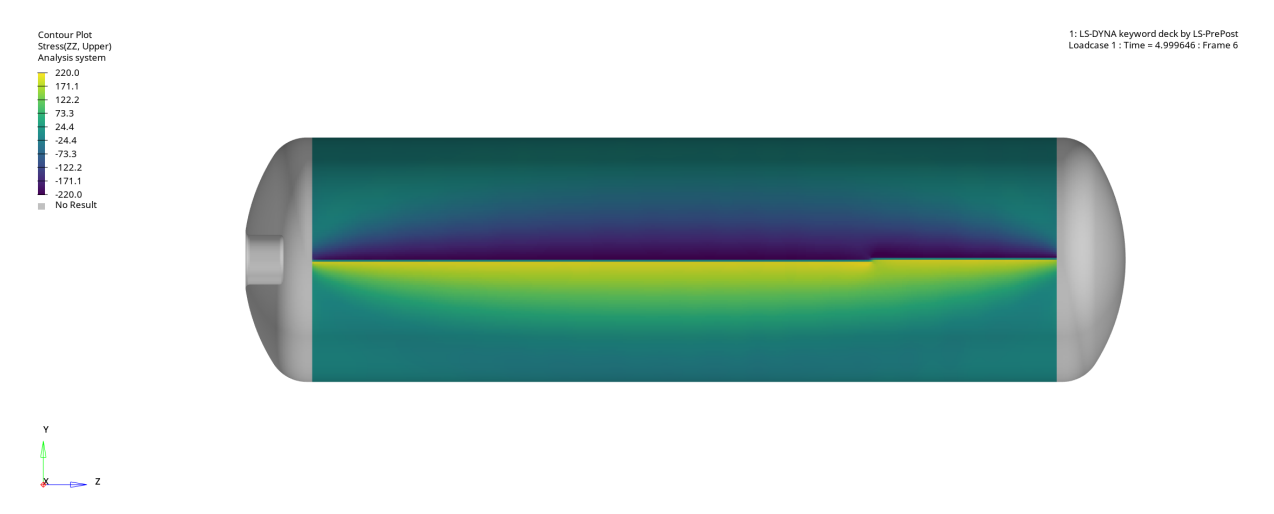


Figure 6.7: Numerical longitudinal stress σ_{zz} under step-wise thermal gradient (tank with normally stiff heads).

As seen in Figure 6.8, the SS-SS analytical prediction reproduces this profile very well. Because the SS-SS beam solution delivers an identical stress distribution at every cross-section, the analytical curve is independent of z, which is consistent with the minor axial variation seen in the FEA. The mid-height values match closely: $-215\,\mathrm{MPa}$ just above and 215 MPa just below the temperature step. At the crown and keel the analytical stresses are 63 MPa and $-63\,\mathrm{MPa}$, higher values than those predicted by the original FEA. It can also be observed that, as we move away from the mid-height, either upwards or downwards, a discrepancy emerges between the stress values obtained from the 2 m tank simulation and those predicted by the analytical model. These differences are attributed to cross-sectional warping, as previously discussed in relation to the vertical displacement curves, or to the influence of boundary conditions near the ends of the cylinder.

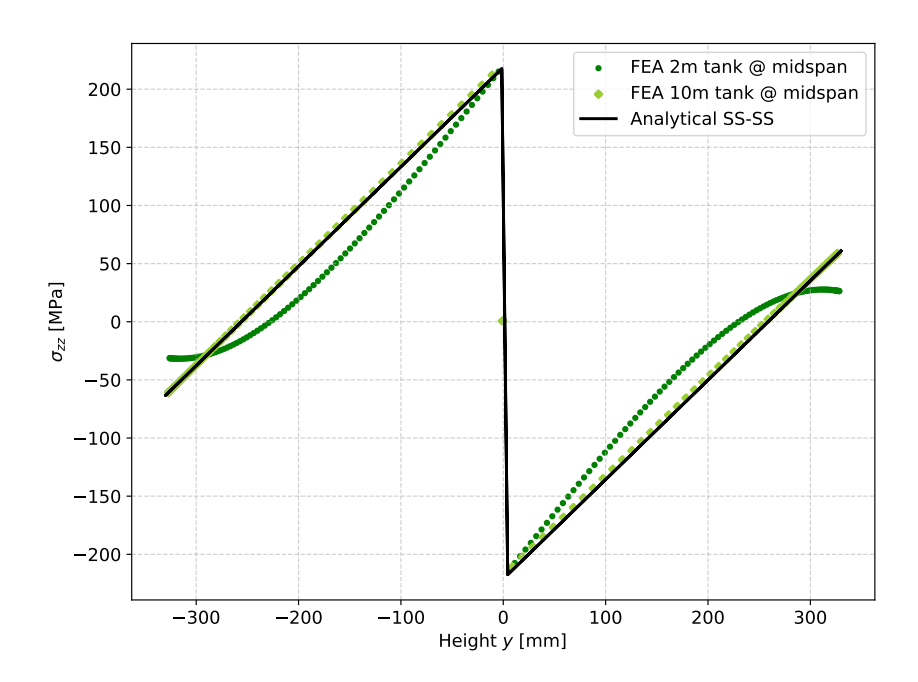


Figure 6.8: Longitudinal stress σ_{zz} as a function of the height for numerical 2m and 10m tanks, and analytical model. Stress at the midspan z=1000mm.

To investigate whether the crown and keel discrepancies arise from the modest length-to-diameter ratio ($L/D \approx 3$) of the original tank, a numerical simulation was conducted with an extended cylindrical section of 10 m, yielding a length-to-diameter ratio of approximately 15. The resulting vertical displacements of crown, mid-height, keel, and cross-sectional average are plotted in Figure 6.9. At first glance the longer shell exhibits an almost uniform deflection over the cross-section, in keeping with classical beam theory. A closer look shows that the residual spread between crown and keel remains on the order of 2 mm to 3 mm, slightly smaller than for the short tank (Figure 6.6) but now negligible when viewed against the 10 m span. Consequently, the simply supported-simply supported (SS-SS) analytical model reproduces the overall bending profile with high fidelity.

Figure 6.8 presents as well the longitudinal stress taken at mid-span of the $10 \,\mathrm{m}$ tank. The distribution is now essentially antisymmetric: $59 \,\mathrm{MPa}$ tension at the crown, $-210 \,\mathrm{MPa}$ compression just above the temperature step, $212 \,\mathrm{MPa}$ tension just below it, and $-61 \,\mathrm{MPa}$ compression at the keel. These values agree closely with the SS-SS analytical prediction in Figure 6.8, whose stress field is independent of the axial coordinate.

The comparison confirms that the earlier discrepancies for the 2 m tank originate from local cross-section deformation that violates the plane-sections assumption of Euler-Bernoulli theory. When the length is increased, cross-section warping vanishes and the analytical model captures both displacement and stress with accuracy.

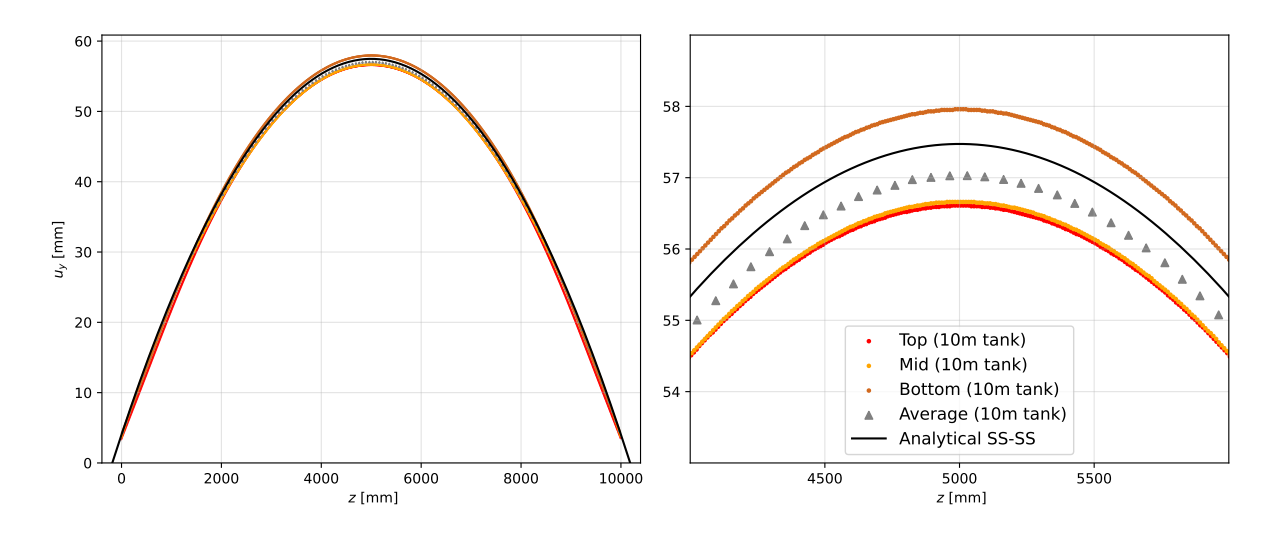


Figure 6.9: Vertical displacement field u_u for a 10 m-long cylinder under the same thermal loading.

6.2.2 Circumferential Stress

Temperature Distribution A

Temperature profile A (see Section 4.2.2) was expanded using fourier series and the coefficients n=0,1 were selected in order to obtain an expression matching the with Eq. (4.30) structure. Because the temperature is uniform through the wall, inner and outer amplitudes are identical, giving $\overline{T}_i = \overline{T}_o = 190\,^{\circ}\text{C}$, $B'_1 = B''_1 = -140\,^{\circ}\text{C}$, and due to the symmetry about the $\varphi = 0$ axis, $D'_1 = D''_1 = 0$.

Figure 6.10 shows the corresponding analytical circumferential stress at the outer layer and focusing only on the midspan cross-section. The solution is antisymmetric, peaking at 3 MPa tension at the crown and -3 MPa compression at the keel, with the mid-height essentially unstressed.

Finite-element results plotted in Figure 6.11a show a significant discrepancy in both magnitude and pattern: the 2 m cylinder exhibits a tensile peak of 48.5 MPa and a compressive minimum of -47.2 MPa, with the locations of tension and compression zones shifted relative to the analytical solution. Two main factors may account for this mismatch. First, the low length-to-diameter ratio ($L/D \approx 3$) makes the stress field highly sensitive to boundary conditions, whereas the analytical model is based on plane thermoelasticity and assumes an infinitely long shell, neglecting boundary effects. Second, the analytical model does not account for the bending component induced by the vertical temperature gradient, which also influences the hoop stress distribution.

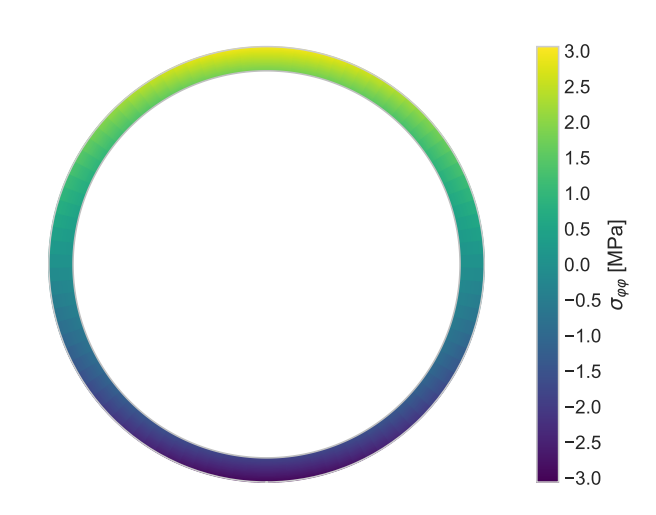


Figure 6.10: Analytical circumferential stress $\sigma_{\varphi\varphi}$ for temperature profile A.

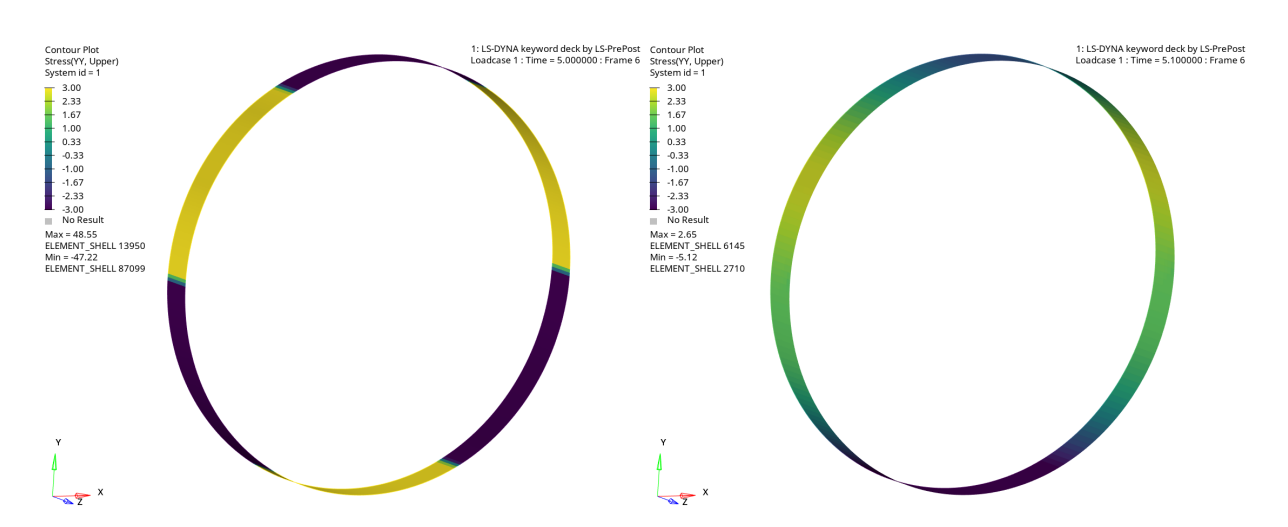


Figure 6.11: Numerical circumferential stress $\sigma_{\varphi\varphi}$ for temperature profile A. Left: 2 m cylinder. Right: 10 m cylinder.

To attenuate edge influences the cylindrical length was increased to $10\,\mathrm{m}$. As Figure 6.11b shows, the peak circumferential stress now falls to about $-5\,\mathrm{MPa}$, i.e. the same order of magnitude predicted by the analytical model. Nevertheless, the spatial distribution still differs: the keel experiences the largest compression, the flanks switch to mild tension, and the crown returns to a small compressive value. Even though the cylinder length was extended to minimize boundary effects, bending remains present due to the physical continuity of the structure. Meaning, the midspan is not isolated from the rest of the cylinder.

This bending behavior violates the plane-stress assumptions underlying the analytical derivation of the analytical circumferential stress. To investigate this effect, an experiment was conducted in which the coefficient of thermal expansion in the longitudinal direction (z) was artificially set to zero. With this modification, the midspan of the 10 m long tank not only exhibited stress magnitudes comparable to those predicted by the analytical model, but also replicated its antisymmetric spatial distribution: tensile stress at the top and compressive stress at the bottom. This confirms that constraining thermal expansion

in the longitudinal direction suppresses bending, allowing the stress state to align more closely with the plane-stress assumption.

Temperature Distribution B

Profile B (Section 3.3) is a smoother linear gradient. The previously explained procedure yields $\overline{T}_i = \overline{T}_o = 190\,^{\circ}\text{C}$ and $B'_1 = B''_1 = -90\,^{\circ}\text{C}$, with $D'_1 = D''_1 = 0$. The analytical circumferential stress, plotted in Figure 6.12, is antisymmetric and very small, reaching only $\pm 2.0\,\text{MPa}$. With the same profile applied to the 2m cylinder the numerical solution in Figure 6.13a is similar to the analytical stress distribution and the values drop to $\pm 1.4\,\text{MPa}$ —one order of magnitude lower than for the step-wise gradient (Profile A) and in excellent agreement with the analytical scale. The 10 m cylinder (Figure 6.13b) yields virtually the same result: compression at the keel, zero stress at mid-height, and tension at the crown, again limited to about $\pm 1.4\,\text{MPa}$.

The previously observed discrepancies can thus be attributed to bending effects, which were amplified by the artificially sharp temperature step assumed in Profile A. When a more realistic, smoothly varying thermal gradient is employed, the influence of thermal bending on the hoop stress becomes negligible. Under these conditions, the assumptions of the two-dimensional thermoelasticity solution remain valid, and the finite element and analytical results show reasonable agreement. Nevertheless, this analysis also reveals that with a smoother and less idealized temperature distribution, the thermally induced hoop stresses are approximately two orders of magnitude smaller than those generated by internal pressure.

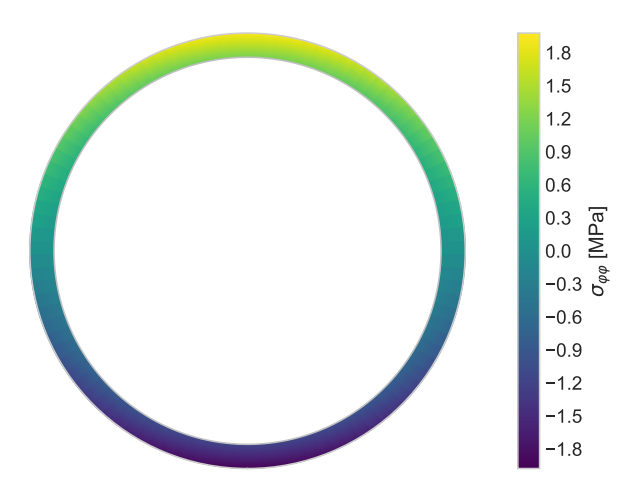


Figure 6.12: Analytical circumferential stress $\sigma_{\varphi\varphi}$ for temperature profile B.

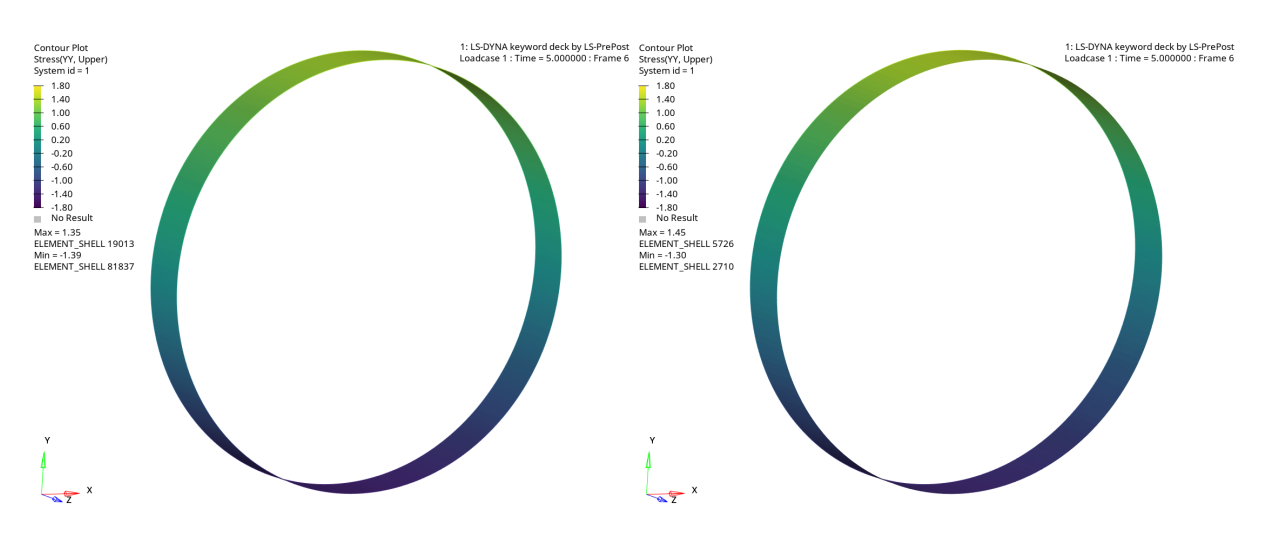


Figure 6.13: Numerical circumferential stress $\sigma_{\varphi\varphi}$ for temperature profile B: Left: 2 m cylinder. Right: 10 m cylinder.

6.2.3 Stress Tensor

The thermal longitudinal stress was reasonably well predicted by the beam model. In contrast, the analytical prediction of the hoop stress is valid only when the assumptions underlying its derivation are approximately satisfied. One key assumption —the plane stress condition— is not applicable in the case of the 2 m tank with temperature profile A. Even at midspan, the influence of both boundary and bending effects remains evident. Additionally, the radial and shear stress components are negligible (not shown for brevity). For these reasons, the chosen analytical thermal stress tensor will be reduced to a single non-zero component in the longitudinal direction.

$$\boldsymbol{\sigma}_{\text{thermal}}^{\text{analytical}} = \begin{bmatrix} \sigma_{\varphi\varphi} & \tau_{\varphi r} & \tau_{\varphi z} \\ \tau_{r\varphi} & \sigma_{rr} & \tau_{rz} \\ \tau_{z\varphi} & \tau_{zr} & \sigma_{zz} \end{bmatrix} = \begin{bmatrix} \sigma_{\varphi\varphi} & 0 & 0 \\ 0 & 0 & 0 \\ 0 & 0 & \sigma_{zz} \end{bmatrix} \approx \begin{bmatrix} 0 & 0 & 0 \\ 0 & 0 & 0 \\ 0 & 0 & \sigma_{zz} \end{bmatrix}. \tag{6.2}$$

6.3 Gravity

As established in Section 6.2, the vessels overall flexure is governed by a simply supported behaviour. The kinematic discussion given earlier therefore applies and is not repeated here. Figure 6.14 presents the longitudinal normal stress obtained from the finite-element model, while Figure 6.15 shows the corresponding simply-supported analytical prediction. The agreement is appropriate: the crown is in compression and the keel in tension, the mid-height is stress-free, and the profiles are nearly symmetric about mid-span.

Quantitatively, the analytical solution gives a peak tension of 1.43 MPa at z=1000 mm; the numerical model yields 1.50 MPa at z=1050 mm. At the weld seams the analytical stresses (± 0.41 MPa) are slightly lower than the numerical values (± 0.61 MPa), but the antisymmetric pattern is preserved.



Figure 6.14: Normal stress σ_{zz} due to effect of gravity: Numerical Model.

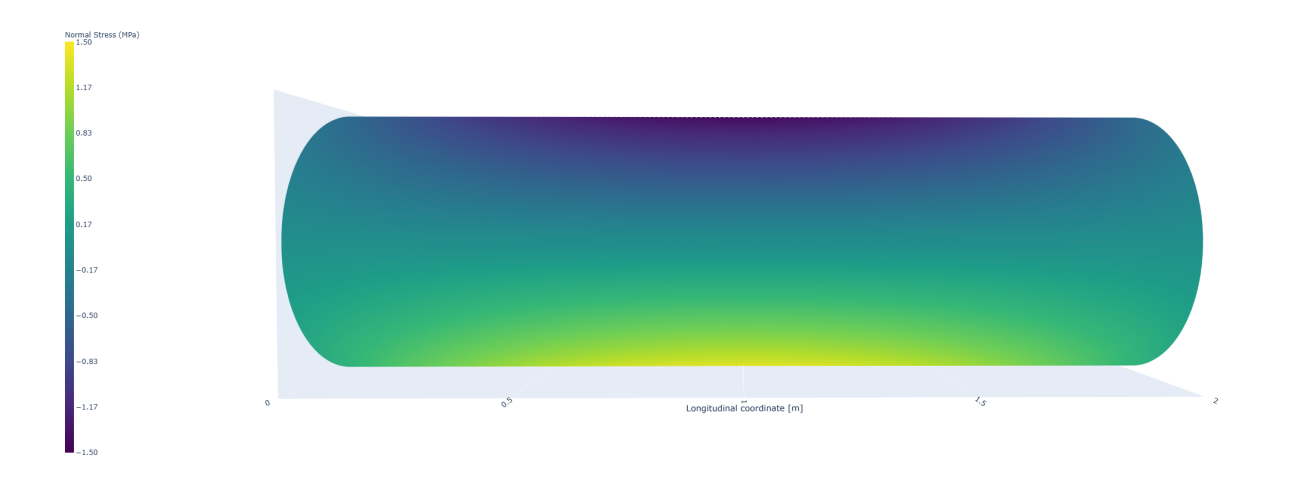


Figure 6.15: Normal stress σ_{zz} due to effect of gravity: Analytical Model.

6.3.1 Stress Tensor

Because these gravity-induced stresses are one to two orders of magnitude smaller than those produced by internal pressure or by thermal gradients (Sections 6.1 and 6.2), the gravitational contribution will be omitted from the combined stress state.

$$\boldsymbol{\sigma}_{\text{gravity}}^{\text{analytical}} = \begin{bmatrix} \sigma_{xx} & \tau_{xy} & \tau_{xz} \\ \tau_{yx} & \sigma_{yy} & \tau_{yz} \\ \tau_{zx} & \tau_{zy} & \sigma_{zz} \end{bmatrix} = \begin{bmatrix} 0 & 0 & 0 \\ 0 & 0 & \tau_{yz} \\ 0 & \tau_{zy} & \sigma_{zz} \end{bmatrix} \approx \begin{bmatrix} 0 & 0 & 0 \\ 0 & 0 & 0 \\ 0 & 0 & 0 \end{bmatrix}.$$
(6.3)

6.4 Superimposition of Loads

Because Section 6.3 showed that gravity-induced stresses are two orders of magnitude lower than those from pressure or temperature, only the pressure and thermal contributions are retained. Since all pertinent stress components are already expressed in the same cylindrical coordinate system, the analytical combined thermo-mechanical stress state can be written as

$$\boldsymbol{\sigma}_{\text{thermomechanical}}^{\text{analytical}} = \underbrace{\begin{bmatrix} \sigma_{\varphi\varphi} & 0 & 0 \\ 0 & 0 & 0 \\ 0 & 0 & \sigma_{zz} \end{bmatrix}}_{\text{pressure}} + \underbrace{\begin{bmatrix} 0 & 0 & 0 \\ 0 & 0 & 0 \\ 0 & 0 & \sigma_{zz} \end{bmatrix}}_{\text{thermal}} + \underbrace{\begin{bmatrix} 0 & 0 & 0 \\ 0 & 0 & 0 \\ 0 & 0 & 0 \end{bmatrix}}_{\text{gravity}}. \tag{6.4}$$

Applying Eq. (2.10) to this tensor yields the von Mises equivalent stress. Figure 6.16 presents the distribution for the coupled finite-element model, and Figure 6.17 shows the coupled analytical prediction.

The numerical model attains a peak von Mises stress of 345 MPa at the left weld seam on the mid-height line where the temperature jump is. The stresses are shown to maintain highest close to the temperature transition zone, and attenuate near the crown and keel of the tank.

The analytical solution captures this global behavior, but displays two local maxima near the boundary: $359\,\mathrm{MPa}$ on the left weld seam $z=0\,\mathrm{mm}$, at a height just above the temperature interface, and $288\,\mathrm{MPa}$ about $70\,\mathrm{mm}$ away from the weld seam, in the lower side of the temperature interface.

The first local maximum occurs at the upper weld seam, where the stress reaches 359 MPa. Axisymmetric-pressure analysis (Figure 6.3) over-predicts compressive longitudinal stress right at the clamp; the thermal field is also compressive in the upper half. Their algebraic combination therefore drives total longitudinal stress high, which drives von Mises stress to a higher value that does not appear in the finite-element result, where cap flexibility moderates the clamp reaction. The difference is not higher since the circumferential stress near the clamp on the numerical model is much higher than the one predicted by the analytical model, which then compensates for the previous longitudinal stress overestimation.

The second peak appears approximately 70 mm from the weld seam, reaching 288 MPa. At this distance, the bending moment from the clamp changes sign: the pressure solution is tensile, and the thermal longitudinal stress is tensile below the interface, so both reinforce each other. This peak matches more closely in magnitude to the value of 265 MPa experienced by the numerical model at this location.

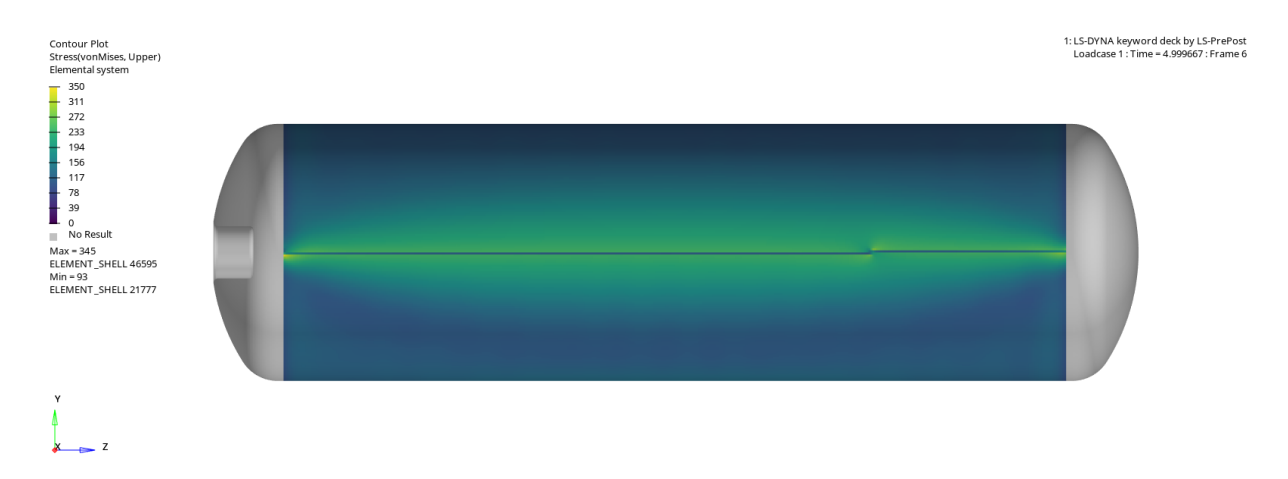


Figure 6.16: Von Mises stress σ_{VM} due to combined pressure and thermal loading: complete numerical model.

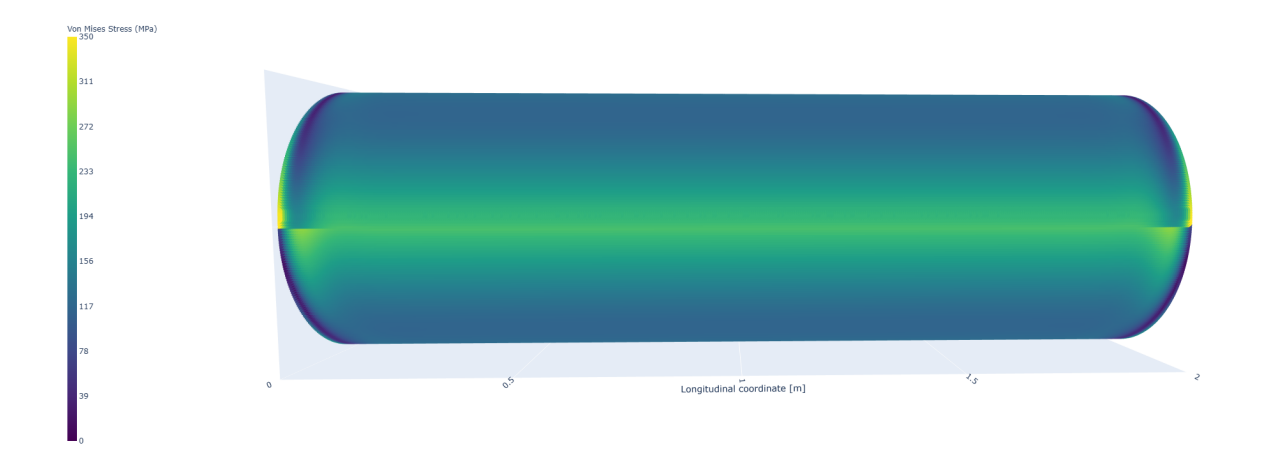


Figure 6.17: Von Mises stress σ_{VM} due to combined pressure and thermal loading: analytical model.

To eliminate boundary effects from the analysis, attention is focused on the midspan region of the vessel. Figure 6.18 compares the von Mises stress distributions obtained from the analytical and numerical models at midspan. The analytical model predicts a peak stress of 245 MPa, while the numerical simulation yields a slightly higher peak of 248 MPa. The corresponding minimum stress values are 107 MPa and 113 MPa, respectively.

It is evident that both models exhibit increasing agreement as one approaches the midheight of the cross-section. This is particularly significant, as the regions near mid-height are where the maximum stresses occur, meaning the analytical model provides reasonable predictions in the most critical areas. Conversely, deviations become more pronounced toward the crown and keel. These discrepancies are primarily attributed to two factors: (1) warping of the cross-section, where the top and bottom fibers exhibit different displacements, and (2) the influence of boundary conditions that introduce localized three-dimensional effects not captured by beam theory.

The figure also highlights a key distinction: the SS-SS analytical model exhibits a perfectly symmetric von Mises stress distribution with respect to the mid-height, whereas the numerical model —while nearly symmetric— shows slight asymmetries near the crown and keel. This asymmetry further underscores the impact of localized three-dimensional effects. Overall, once edge-induced deviations are excluded, the coupled analytical formulation demonstrates good agreement with the finite element results in the regions of primary interest.

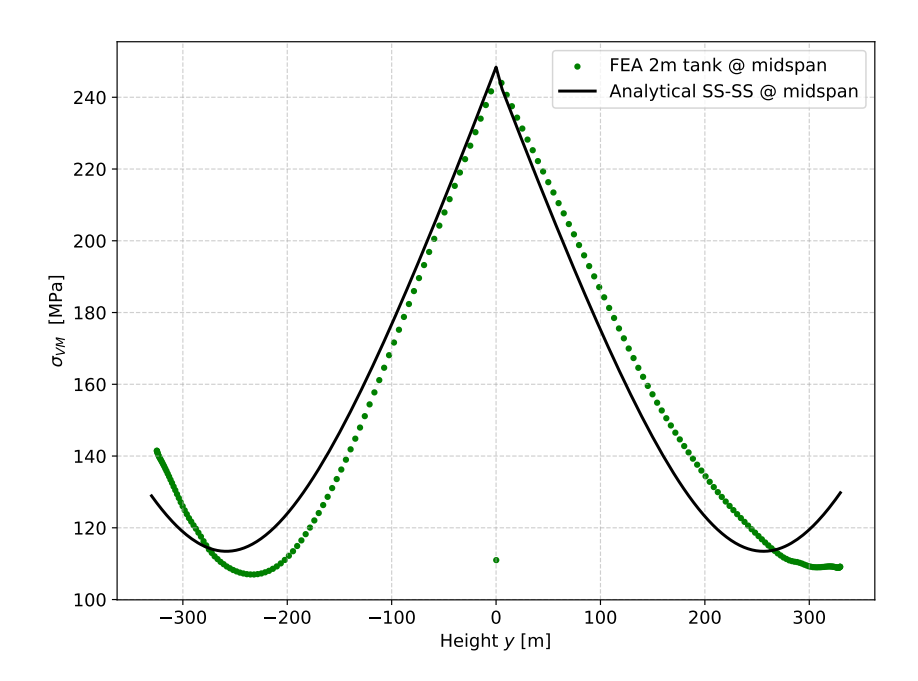


Figure 6.18: von Mises stress σ_{VM} for combined loading at the midspan: numerical and analytical model.

6.5 Summary of stress components

Table 6.2 provides a summary of the main stress quantities compared between the analytical and numerical models. It begins with a comparison at the midspan and midheight. It is important to note that the results for the pressure model are axisymmetric, meaning that the vertical position does not influence the stress distribution. The midheight was selected as the reference location for the table, as it exhibits the higher stresses for the thermal longitudinal model. For the gravity load case, the stress is zero at the midspan-midheight location, which is therefore chosen as a natural reference point.

Regarding the extreme values (i.e., absolute maximum stresses), it is important to high-light that these may occur at different locations along the tank, either longitudinally or vertically. The specific positions of these maxima are discussed in detail within each corresponding subsection. The purpose of the table is to provide a global overview of the maximum stress values to help guide the reader through the key results.

Table 6.2: Comparison between FEA and analytical results at midspan-midheight and at maximum locations (all values in MPa).

Load Case	Model	Quantity	${f FEA} \ {f Result}$	Analytical Result	Difference
Midspan - Midheight					
Pressure	Shell Model	σ_{zz}	65.5	65	0.5
		$\sigma_{arphiarphi}$	131	131	0
		σ_{zr}	0	0	0
Thermal Longitudinal	Beam Model	σ_{zz}	216	215	1
Thermal Circumferential	Shell Model	$\sigma_{arphiarphi}$	0	0	0
Gravity	Beam Model	σ_{zz}	0	0	0.07
Superimposed		σ_{VM}	248	245	3
Extreme - Location In	ndependent				
Pressure	Shell Model	σ_{zz}	100	-136	236
		$\sigma_{arphiarphi}$	140	135	5
		σ_{zr}	1.2	10	8.8
Thermal Longitudinal	Beam Model	σ_{zz}	216	215	1
Thermal Circumferential	Shell Model	$\sigma_{arphiarphi}$	-47.2	-5	42.2
Gravity	Beam Model	σ_{zz}	1.5	1.43	0.07
Superimposed		σ_{VM}	345	359	14

7. Conclusion

This thesis investigated the accuracy and applicability of simplified analytical models for predicting the thermo-structural response of a cryogenic pressure vessel during the cooldown phase. The central research question was: Can analytical models predict the spatial variation and peak stress values that develop during the cooldown of cryogenic tanks with sufficient accuracy for preliminary design purposes?

To address this question, a reduced-order analytical model was developed and benchmarked against detailed finite element analyses (FEA) using shell elements. The reference geometry corresponds to a stainless-steel cylinder with torispherical heads, based on the demonstrator from the Horizon Europe project ALRIGH2T. The load case included internal pressure, vertical temperature stratification, and self-weight. All materials were idealised as linear-elastic and temperature-independent.

The analytical shell model proved capable of accurately predicting both circumferential and longitudinal stresses arising from internal pressure. In the mid-span region—sufficiently far from boundary effects— the discrepancy between the analytical and numerical results was less than 1%. At the boundaries, the analytical model yielded conservative stress predictions, a result attributed to the replacement of the elastic torispherical caps with idealised constraints that artificially increased the local stiffness of the model. For instance, the analytical model predicted a peak stress of $-136 \,\mathrm{MPa}$ compared to the FEA result of $130 \,\mathrm{MPa}$.

Under thermal loading from a vertical temperature gradient, the beam model effectively captured the longitudinal thermal stresses. Using an idealised step-wise temperature profile, it successfully reproduced the four-zone axial stress distribution observed in the FEA. However, the model did not account for cross-sectional warping effects, which become significant in cylinders with moderate length-to-diameter ratios. This limitation accounts for the discrepancies observed between the analytical and numerical stress predictions at the keel and crown of the tank. Nevertheless, the maximum longitudinal thermal stress, found at the mid-span and mid-height, was captured with accuracy, showing a deviation of only 1 MPa from the numerical result.

For the vertical temperature gradient, the results indicate that the 2D thermoelastic analytical model is not suitable for predicting the circumferential stress in the present case study. Even at the tank's mid-span —the intended region of applicability for the model—the fundamental assumption of plane stress is violated. As a result, the analytical predictions are not representative of the actual stress state. The mid-span region experiences thermally induced bending effects that significantly influence the circumferential stress distribution, and these are not captured by the simplified model.

Additionally, the analyses show that although the beam model accurately estimates stresses arising from gravity, the maximum value remains below 2 MPa. This contribution is therefore negligible compared to the stress levels induced by pressure and thermal loads. In summary, the models deemed applicable for predicting the superimposed stress state were the shell model, used to estimate both longitudinal and circumferential stresses under internal pressure, and the beam model, which provided reasonable predictions of longitudinal thermal stresses.

Under combined pressure and thermal loading, the coupled analytical formulation matched the mid-span von Mises stress to within 1% of the numerical reference (FEA: 248 MPa, analytical: 245 MPa). At the weld seams, where the global maximum occurs, the analytical model yielded a conservative estimate of 359 MPa, compared to the FEA result of 345 MPa.

These findings confirm that the analytical models developed in this work are capable of capturing the stress distribution and peak values with an accuracy that meets the requirements of preliminary design. The conservative overestimation at structural discontinuities such as weld seams is acceptable at this design stage. Overall, the analytical approach provides a fast and sufficiently accurate method for early-stage structural assessment of cryogenic vessels subject to cooldown conditions.

Naturally, the scope of the study was limited. Linear elasticity and temperature-independent properties ignore the stiffening that stainless steels experiences as temperature decreases. Axisymmetric pressure and purely vertical temperature gradients neglect sloshing, circumferential stratification, and radial conduction. Cross-section warping and shear deformation were omitted, although their influence becomes non-trivial for very short or thick-walled vessels. Finally, the analysis was quasi-static; fatigue and transient fill-drain cycles remain unaddressed.

From a geometrical standpoint, the base configuration reflects dimensions representative of industrial practice. Two primary parameters were varied to assess their impact on the structural response. First, the length-to-diameter ratio, which was increased from 3 to 15 to examine the validity of beam theory for slender tanks. Second, the stiffness of the torispherical end caps, comparing elastic behavior to an idealized perfectly rigid condition, to evaluate the influence of boundary condition modeling. While these variations provided valuable insights, further parametric studies, such as varying wall thickness or analyzing tanks with lower slenderness ratios, would help clarify the applicability limits of thin-shell and beam models. Different geometrical configurations are expected to exhibit varying degrees of agreement with analytical formulations, thus highlighting the importance of model selection in the context of design accuracy.

Building on the present foundation, future work could (i) incorporate torispherical-head compliance directly, perhaps through boundary-layer superposition or shell-of-revolution theory; (ii) introduce temperature-dependent material data and extend the solver to elastoplastic regimes validated against cryogenic experiments; (iii) couple the stress formulation with one-dimensional transient heat-transfer models to predict the full cool-down history rather than the worst extremes; (iv) instrument a full-scale demonstrator -such as the ALRIGH2T vessel- and compare measured strains with the rapid solver.

Bibliography

- [1] R. F. Barron, *Cryogenic Systems*, 2nd ed., ser. Monographs on Cryogenics. New York, NY: Oxford University Press, Jun. 1985.
- [2] Y. Ma, K. Zhu, Y. Li, and F. Xie, "Simulation on chill-down behavior and induced thermal stress of a cryogenic tank during ln2 filling," *Applied Thermal Engineering*, vol. 181, 11 2020.
- [3] K. Zhu, Y. Li, Y. Ma, J. Wang, L. Wang, and F. Xie, "Influence of filling methods on the cool down performance and induced thermal stress distribution in cryogenic tank," *Applied Thermal Engineering*, vol. 141, p. 10091019, Aug. 2018. [Online]. Available: http://dx.doi.org/10.1016/j.applthermaleng.2018.06.030
- [4] Alrigh2t, "Alrigh2t engineering, research, and design," 2025, accessed: 2025-03-27. [Online]. Available: https://alrigh2t.eu/
- [5] L. Keller, J. Klebanoff, "The need for hydrogen-based energy technologies in the 21st century," in *Hydrogen Storage Technology: Materials and Applications*, L. Klebanoff, Ed. Boca Raton: CRC Press, 2013, pp. 3–30. [Online]. Available: https://www.taylorfrancis.com/books/edit/10.1201/b13685/hydrogen-storage-technology-lennie-klebanoff
- [6] W. Wentz, R. Myose, and A. Mohamed, "Hydrogen-fueled general aviation airplanes," in 43rd AIAA Aerospace Sciences Meeting and Exhibit, Reno, Nevada, 2005. [Online]. Available: https://arc.aiaa.org/doi/10.2514/6.2005-7324
- [7] C. Winnefeld, T. Kadyk, B. Bensmann, U. Krewer, and R. Hanke-Rauschenbach, "Modelling and designing cryogenic hydrogen tanks for future aircraft applications," *Energies*, vol. 11, no. 1, p. 105, 2018. [Online]. Available: https://www.mdpi.com/ 1996-1073/11/1/105
- [8] S. K. Mital, J. Z. Gyekenyesi, S. M. Arnold, R. M. Sullivan, J. M. Manderscheid, and P. L. N. Murthy, "Review of current state of the art and key design issues with potential solutions for liquid hydrogen cryogenic storage tank structures for aircraft applications," NASA Glenn Research Center, Cleveland, OH, United States, Technical Memorandum NASA/TM-2006-214346, 2006. [Online]. Available: https://ntrs.nasa.gov/citations/20060056194
- [9] L. Bowman, B. Klebanoff, "Historical perspectives on hydrogen, its storage, and its applications," in *Hydrogen Storage Technology: Materials and Applications*, L. Klebanoff, Ed. Boca Raton: CRC Press, 2013, pp. 65–90.

- [Online]. Available: https://www.taylorfrancis.com/books/edit/10.1201/b13685/hydrogen-storage-technology-lennie-klebanoff
- [10] A. Zttel, A. Remhof, A. Borgschulte, and O. Friedrichs, "Hydrogen: the future energy carrier," *Philosophical Transactions of the Royal Society A: Mathematical, Physical and Engineering Sciences*, vol. 368, no. 1923, pp. 3329–3342, 2010. [Online]. Available: https://doi.org/10.1098/rsta.2010.0113
- [11] S. Petitpas, G. Aceves, "Hydrogen storage in pressure vessels: Liquid, cryogenic, and compressed gas," in *Hydrogen Storage Technology: Materials and Applications*, L. Klebanoff, Ed. Boca Raton: CRC Press, 2013, pp. 91–108. [Online]. Available: https://www.taylorfrancis.com/books/edit/10.1201/b13685/hydrogen-storage-technology-lennie-klebanoff
- [12] G. D. Brewer, *Hydrogen Aircraft Technology*, 1st ed. New York: Routledge, 1991. [Online]. Available: https://doi.org/10.1201/9780203751480
- [13] T. Flynn, Cryogenic Engineering, Revised and Expanded, 2nd ed. CRC Press, 2020, revised and Expanded. [Online]. Available: https://www.routledge.com/ Cryogenic-Engineering-Revised-and-Expanded/Flynn/p/book/9780367578169
- [14] A. Gomez and H. Smith, "Liquid hydrogen fuel tanks for commercial aviation: Structural sizing and stress analysis," *Aerospace Science and Technology*, vol. 95, p. 105438, 2019. [Online]. Available: https://www.sciencedirect.com/science/article/pii/S1270963818304139
- [15] American Society of Mechanical Engineers, BPVCSection VIII-Rules DivisionASME, for Construction ofPressure Vessels 1. 2025. line]. Available: https://www.asme.org/codes-standards/find-codes-standards/ bpvc-viii-1-bpvc-section-viii-rules-construction-pressure-vessels-division-1/2025/ print-book
- [16] International Organization for Standardization, "Iso 20421-1:2019 cryogenic vessels large transportable vacuum-insulated vessels. part 1: Design, fabrication, inspection and testing," https://www.iso.org/standard/68589.html, 2019, accessed: 2025-05-03.
- [17] V. Molkov, H. Ebne-Abbasi, and D. Makarov, "Liquid hydrogen refuelling at hrs: Description of slh2 concept, modelling approach and results of numerical simulations," *International Journal of Hydrogen Energy*, 2024. [Online]. Available: https://doi.org/10.1016/j.ijhydene.2024.10.392
- [18] E. Pizzutilo, T. Acher, B. Reuter, C. Will, and S. Schfer, "Subcooled liquid hydrogen technology for heavy-duty trucks," World Electric Vehicle Journal, vol. 15, no. 1, p. 22, 2024, this article belongs to the Special Issue EVS36International Electric Vehicle Symposium and Exhibition (California, USA). [Online]. Available: https://doi.org/10.3390/wevj15010022
- [19] CEP. White Paper, "sLH2 Fueling SpecificationRelease 1.8," 2021, available online: https://cleanenergypartnership.de/wp-content/uploads/2022/03/

- CEP_20210914_Whitepaper_sLH2-Fueling-Specification_Release_1.8_clean-min.pdf (accessed on 14 May 2025).
- [20] Y. Ma, K. Zhu, and Y. Li, "Numerical investigation on chill-down and thermal stress characteristics of a lh2 tank during ground filling," *International Journal of Hydrogen Energy*, vol. 45, no. 46, pp. 25344–25356, 2020. [Online]. Available: https://www.sciencedirect.com/science/article/pii/S0360319920321935
- [21] K. Zhu, Y. Li, Y. Ma, L. Wang, F. Xie, and J. Wang, "Experimental study on cool down characteristics and thermal stress of cryogenic tank during ln2 filling process," *Applied Thermal Engineering*, vol. 130, pp. 984–994, 2018. [Online]. Available: https://doi.org/10.1016/j.applthermaleng.2017.11.079
- [22] M. Xia, W. Yuan, Q. Zhang, Y. Zheng, P. Li, J. Chen, and J. Xie, "Experimental and numerical analysis of the chill-down process of a large horizontal cryogenic storage tank," *Applied Thermal Engineering*, 2023. [Online]. Available: https://doi.org/10.1016/j.applthermaleng.2023.121246
- [23] S. P. Timoshenko, History of Strength of Materials: With a Brief Account of the History of Theory of Elasticity and Theory of Structures. New York: McGraw-Hill, 1953.
- [24] S. Timoshenko and J. N. Goodier, *Theory of Elasticity*, 2nd ed. McGraw-Hill Book Company, 1951, vol. 49.
- [25] S. P. Timoshenko and S. Woinowsky-Krieger, Theory of Plates and Shells, 2nd ed. New York: McGraw-Hill, 1959.
- [26] J. M. Baker, "Preliminary thermal stress analysis of a high-pressure cryogenic storage tank," Louisiana Tech University, Ruston, LA, United States, Technical Report SE-2003-06-0043-SSC, July 2003. [Online]. Available: https://ntrs.nasa.gov/ citations/20030068185
- [27] A. S. Tsybenko, B. A. Kuranov, A. D. Chepurnoi, V. A. Shaposhnikov, and N. G. Krishchuk, "Thermal stress state of cryogenic high-pressure vessels during chilling and pressurization. report no. 1. method of calculation," *Strength Mater.*, vol. 18, no. 1, pp. 87–92, Jan. 1986.
- [28] R. B. Hetnarski and M. R. Eslami, *Thermal Stresses: First 125 Years of Research* (from 1837 to Approximately 1962). Dordrecht: Springer Netherlands, 2014, pp. 5457–5468. [Online]. Available: https://doi.org/10.1007/978-94-007-2739-7_977
- [29] L. Nappa, Thermal Stresses in Elastic Cylinders and Circular Shells. Dordrecht: Springer Netherlands, 2014, pp. 5344–5369. [Online]. Available: https://doi.org/10. 1007/978-94-007-2739-7_298
- [30] B. A. Boley and J. H. Weiner, *Theory of Thermal Stresses*, ser. Dover Civil and Mechanical Engineering Series. Dover Publications, 1997.

- [31] R. B. Hetnarski and M. R. Eslami, *Thermal StressesAdvanced Theory and Applications*, 2nd ed., ser. Solid Mechanics and Its Applications. Cham: Springer Nature Switzerland, 2019, vol. 158. [Online]. Available: https://doi.org/10.1007/978-3-030-10436-8
- [32] C. H. Kent, "Thermal stresses in thin-walled cylinders," *Transactions of the ASME*, vol. 53, no. 2, pp. 167–179, 1931, published online April 17, 2023. [Online]. Available: https://doi.org/10.1115/1.4022678
- [33] J. N. Goodier, "Thermal stress in long cylindrical shells due to temperature variation round the circumference, and through the wall," *Canadian Journal of Research*, vol. 15a, no. 4, pp. 49–58, 1937. [Online]. Available: https://doi.org/10.1139/cjr37a-008
- [34] G. Sauer, "Simple formulae for the approximate computation of axial stresses in pipes due to thermal stratification," *International Journal of Pressure Vessels and Piping*, vol. 69, no. 3, pp. 213–223, 1996. [Online]. Available: https://www.sciencedirect.com/science/article/pii/0308016195001344
- [35] M. A. Irfan and W. Chapman, "Thermal stresses in radiant tubes due to axial, circumferential and radial temperature distributions," *Applied Thermal Engineering*, vol. 29, no. 10, pp. 1913–1920, 2009. [Online]. Available: https://www.sciencedirect.com/science/article/pii/S1359431108003621
- [36] W. Logie, J. Pye, and J. Coventry, "Thermoelastic stress in concentrating solar receiver tubes: A retrospect on stress analysis methodology, and comparison of salt and sodium," *Solar Energy*, vol. 160, pp. 368–379, 2018. [Online]. Available: https://api.semanticscholar.org/CorpusID:125973287
- [37] A. Montoya, M. Rodrguez-Snchez, J. Lpez-Puente, and D. Santana, "Numerical model of solar external receiver tubes: Influence of mechanical boundary conditions and temperature variation in thermoelastic stresses," *Solar Energy*, vol. 174, pp. 912–922, 2018. [Online]. Available: https://www.sciencedirect.com/science/article/pii/S0038092X18309629
- [38] W. F. Hosford, *Mechanical Behavior of Materials*, 2nd ed. Cambridge: Cambridge University Press, 2009, online publication date: June 2012. [Online]. Available: https://doi.org/10.1017/CBO9780511810923
- [39] G. E. Dieter, Mechanical Metallurgy, si metric edition ed., ser. McGraw-Hill Series in Materials Science and Engineering. London: McGraw-Hill, 1988, adapted by David J. Bacon.
- [40] A. C. Ugural and S. K. Fenster, Advanced mechanics of materials and applied elasticity, 5th ed. Philadelphia, PA: Prentice Hall, Jun. 2011.
- [41] Thermophysical Properties of Matter Database (TPMD), "Material properties: 316 stainless," https://trc.nist.gov/cryogenics/materials/316Stainless/316Stainless_rev.htm, 2024, accessed: 2025-05-04.

- [42] J. Freund, "Beam, plate and shell models: Lecture notes," Espoo, Finland, 2025, lecture notes for the course "Beam, Plate and Shell Models", Senior University Lecturer, Aalto University, Espoo, Finland.
- [43] M. R. Eslami, R. B. Hetnarski, J. Ignaczak, N. Noda, N. Sumi, and Y. Tanigawa, Theory of Elasticity and Thermal Stresses: Explanations, Problems and Solutions, ser. Solid Mechanics and Its Applications. Springer Netherlands, 2013, vol. 197. [Online]. Available: https://link.springer.com/book/10.1007/978-94-007-6356-2
- [44] R. C. Hibbeler, *Mechanics of Materials, SI Edition*, 11th ed. Pearson Education Limited, 2023.
- [45] D. Madier, Practical Finite Element Analysis for Mechanical Engineers. Dominique Madier, 2021, hardcover, 663 pages.
- [46] P. M. Kurowski, Finite Element Analysis for Design Engineers, 3rd ed. Warrendale, PA: SAE International, 2022.
- [47] LSTC, LS-DYNA Theory Manual, Livermore Software Technology Corporation, 2023, draft Version. [Online]. Available: https://ftp.lstc.com/anonymous/outgoing/web/ls-dyna_manuals/DRAFT/DRAFT_Theory.pdf